Numerical renormalization group calculations for Kondo-type models of spin clusters on a nonmagnetic metallic substrate

Dissertation

vorgelegt von
Henning-Timm Langwald

betreut durch
Prof. Dr. Jürgen Schnack

Universität Bielefeld
Fakultät für Physik

January 2018

Contents

Acknowledgements

Before the presentation of the actual work, I would like to thank the following people:

Jürgen Schnack

Prof. Schnack has always had time for me and the discussions with him have greatly helped me. Furthermore as my adviser he has always supported me, especially when I needed it the most.

Martin Höck

Martin has been the very best teacher to introduce me to the numerical renormalization group. He has been a great help in the discussions we had and has left me notes which were influential on my work. Furthermore his thesis has proven invaluable as a guide to writing the necessary programs. His attention to even the smallest detail was impressive.

Heinz-Jürgen Schmidt

Apl. Prof. Schmidt has greatly helped me by suggesting a method for solving a rather complex integral.

Felix Kaiser

Felix has been a great colleague and discussing results and methods with him has been most beneficial.

Hanne Litschewsky

Hanne is right at the center of E5 and always looking out for everyone while managing her work. Her friendliness creates a special atmosphere for the whole floor.

Vanessa Homburg

My girlfriend has always been there for me and has shown great patience and tolerance with me during this work.

My parents

They have always supported my choices and been there for me when I needed them.

My former professors and teachers

From the beginnings at school to finishing this thesis is a long time and I think it is important to acknowledge that to obtain the necessary set of skills for this work requires the commitment of many persons who all have greatly contributed to my education.

Furthermore I would like to thank the German Research Foundation (**Deutsche Forschungsgemeinschaft**) for their support through Research Unit 945 (Forschergruppe FOR 945) and the Leibniz Computing Center (**Leibniz-Rechenzentrum**) in Garching for providing computing time.

1 Overview

This thesis is centered around numerical renormalization group (NRG) calculations for spin clusters on nonmagnetic metallic surfaces. The numerical calculations were performed using a program specifically designed for and developed within the research for the thesis. The overall goal is to further the understanding of a potentially crucial interaction, described by a Kondo-type model, of magnetic molecules with a substrate. The main focus is to explore the effect of the strength of this interaction on the magnetization of the deposited spin clusters. The thesis as a whole is subdivided so that different aspects of the goal can be addressed in different chapters. The introduction in chapter 2 serves to provide the reader with the viewpoint this thesis is conducted from and thus allows the reader to understand the chosen methodology. It furthermore presents an overview of the history of the methods used within this thesis so that a context of research is given within which this thesis can be understood. Finally the chapter summarizes aspects of said research to enable readers without prior knowledge to understand the important aspects of the later calculations. Chapter 3 covers the theoretical background of the calculations. As extensive literature detailing the methodology already exist it aims to provide the reader with an overview of obtaining the model and enabling numerically feasible calculations. To this end the chapter highlights the key steps in the process. The excursus in chapter 4 can be seen as an extension to the methodology of the theoretical work of the previous chapter and aims to provide the reader with an outlook of the theoretical work required to extent the calculations to the interactions involving two spin systems on a square lattice. With the overview of the theoretical framework completed chapter 5 presents the reader the results of the numerical renormalization group calculations. At the center of the chapter and thus this thesis is an in-depth analysis of observables for a three spin system affected by its coupling to a nonmagnetic metallic substrate. The following chapter 6 complements the previous one and instead of focusing on the details it presents an analysis of the different scales involved in the calculations. The goal of this is to enable the reader to extend the insight gained by the calculations to a broader range of systems. Finally a summary is given in chapter 7. The appendix provides the technical details for a necessary calculation in the excursus and shows observables of additional systems.

2 Introduction

2.1 Starting point

To understand the methodology used in this thesis as well as the viewpoint on the questions addressed this chapter outlines the starting point from which we begin our investigation. This is namely the wider topic of magnetic molecules (MM), which are at the center of interest for our research group. Magnetic molecules as a modern field of research became popular with the discovery of a hysteresis of purely molecular origin in Mn$_{12}$ac [1, 2]. This gave rise to the idea that such molecules could be used in information technology. With the ultimate goal of storing information only within a single molecule [3] the possible use of such molecules as means of miniaturization could increase the storage density of mass storage devices massively. Furthermore magnetic molecules are candidates to enable the fabrication of qubits which would be essential parts in the construction of so called quantum computers [4]. With these possible applications in mind a lot of research has been conducted on investigating the properties of such molecules and in an interdisciplinary field of research shared between physics and chemistry on the synthesis of molecules with desirable qualities [1, 2]. For the understanding of the parameters of future chapters it is noteworthy here, that these qualities, such as a stable magnetization of a single molecule appear at very low temperatures [3]. This requires, additionally to the treatment in the framework of quantum mechanics, that one considers other possible effects at these temperatures that might affect the molecules in the greater context of their application in future information technology or the study of their properties. In the past properties of such molecules have often been determined in bulk samples using experimental techniques which were meant to ensure that single molecule properties were extracted nonetheless [2]. Our research group has been studying properties of such molecules theoretically in the framework of statistical quantum mechanics [2] using the observables of such systems for their characterization. The molecules themselves being described by modified Heisenberg Hamiltonians with all due restrictions on applicable systems that come with it. However for their future applications such molecules would most likely have to be addressed individually giving rise to an interest in their properties specifically when deposited on a substrate. More recent experiments have allowed to study individual molecules or atoms under these circumstances by means of e.g. spin-polarized scanning tunneling spectroscopy [5]. Given the history of our research group in characterizing the properties of such molecules by studying the system observables the natural question arises how such properties might be altered by depositing a single molecule on a nonmagnetic metallic substrate. Arriving here we have the starting point to our investigation. A single magnetic molecule, theoretically characterized by its Hamiltonian, a nonmagnetic metallic surface, some form of interaction between them and a special interest in the observables of the magnetic molecule at different temperatures and in an external magnetic field. This starting point however would still encompass all possible interactions the magnetic molecule might have with the substrate. I in this thesis choose to focus on a subset of those interactions by making limiting assumptions on the interactions that we want to include. Given that we come from a background of characterizing magnetic molecules by their respective Hamiltonian I choose to specifically study interactions where said Hamiltonian can be used to describe the molecule whether it is interacting with the substrate or not. This means that the fundamental structure and inner interactions of the molecule are not altered by the interaction with the substrate. Now we need to specify our model for the nonmagnetic metallic surface and its interaction with the molecule. This is now the point where one might look at similar problems in physics history and find that magnetic impurities within a nonmagnetic metal have been treated within the greater context of the Kondo model. Before we focus more on that we sum up our ideas for modeling our problem. We choose to describe a magnetic molecule deposited on a nonmagnetic metallic surface via a Hamiltonian consisting of three parts. One representing the magnetic molecule, one representing the substrate as a conduction band and one representing their interaction. Now for our numerical calculations later we specifically choose a Heisenberg Spin Hamiltonian for the molecule and a Kondo like coupling Hamiltonian for the interaction between substrate and molecule, but we stress that a wider variety of molecule Hamiltonians and a wider variety of coupling interactions can be described within the general framework of the numerical treatment (as one may assess by following the complete derivation of it in [6]).

2.2 From the Kondo problem to Wilson's NRG

Now that we have chosen to work on our problem using a Kondo like model, we take a short look at its history. The model itself is named after Jun Kondo. The problem that he tackled was a local minimum for resistance versus temperature at low temperatures for what he described as dilute magnetic alloys [7]. The problem originated from experiments then dating back three decades when measurements on several metals, among them notably gold, were performed and a local minimum of resistance was found that was not fully understood within existing theory [8]. Already then it was known that the gold wire used for the experiment featured a concentration of impurities and a potential connection between the resistance minimum and the impurity of the sample was hinted at. Kondo based his theoretical attempt on the s-d exchange model, which had been developed in the two decades prior and been applied in the same greater context [9, 10, 11, 12]. Kondo focused on the impurities and chose to treat these impurities due to their low density within the metal as practically uncorrelated. With prior research done on the formation of local moments, notably by Anderson [13] and Wolff [14], Kondo focused on these to describe the impurities. This allowed him to view the problem as that of a single magnetic impurity within a nonmagnetic metallic host. Describing it with a localized spin S coupled to non-interacting delocalized electrons via an exchange interaction J (cf. J_A within the context of this thesis) he then approached the problem within perturbation theory and was able to sufficiently explain the resistance minimum with an antiferromagnetic J. He, based on fitting to data, estimated its strength to about $0.2eV$. Later it was shown by Schrieffer and Wolff, that the Hamiltonians used by Kondo and Anderson, who described the impurities via orbitals that can be occupied by electrons, are equivalent for those conditions most favorable for the formation of local moments and thus that the two models are closely related [15]. Due to the historical name "impurity" within the original problem we will in the subsequent parts of this thesis often refer to the deposited molecule (or its respective Hamiltonian) as the impurity. Anderson in his famous "poor man's scaling" investigated the scaling properties of the problem further but experienced, that the perturbative treatment of the problem breaks down at lower temperatures where, as it turned out, the exchange coupling can no longer be treated as a small perturbation [16]. However this break-down can be used to define a scale, the Kondo temperature T_K, which for the context of this thesis we will expand upon in chapter 2.4. Thus a new approach was needed to access the physics below said temperature scale. This was achieved by Kenneth Wilson about a decade after Kondo's original work. His solution is notable for the use of computers, the discretization of the continuous energy of the conduction band and the inherent use of scaling within the solution. All of these culminated in his numerical renomalization group (NRG), an approximate numerical method, that he used to treat the problem of the interaction between impurity and electrons non-perturbatively [17]. Since the numerical calculations in this thesis are based on the NRG as invented by Wilson most of the theory in chapter 3 focuses on the NRG and will provide further inside. Reference [18] can serve the reader as an additional source for an introduction.

2.3 Further developments

After Wilson's original paper his approach was notably extended to the Anderson model in cooperation with Krishna-murthy and Wilkins [19, 20]. An extensive review in 2008 of further progress in the context of the NRG was created by Bulla, Costi and Pruschke [21]. Of most relevance for this thesis are the several improvements made to the original NRG, that increase numerical accuracy. Notably there is the z-averaging introduced by Oliveira and Oliveira [22, 21], that is used for the numerical calculations in this thesis. Furthermore Campo and Oliveira introduced changes to the discretization scheme [23, 24], which finally led to an improved discretization by Zitko and Pruschke [25, 26], which is used for the calculations presented in chapter 5. An overview over these discretization schemes, as well as the technical details to implement them, is part of reference [6] by Höck. Development at the time of the work on this thesis could also make multichannel NRG calculations (i.e. those involving more than one Wilson chain, see chapter 3) less resource demanding [27]. Additionally the normalization factors, as expanded upon in the excursus in chapter 4, gained some attention [28].

On the experimental site it became possible to investigate single atoms at low temperatures via scanning tunneling microscopy (STM) [29] and spectroscopy (STS) on surfaces. This allowed measurements of the Kondo effect via its resonance on the current [30, 31]. More recently it became possible to measure single adatoms on non-magnetic metallic surfaces in an outer magnetic field by spin-polarized scanning tunneling spectroscopy (SP-STS), thus allowing focus on spin properties on single atom scale [32, 33]. A review for the technique can be found in reference [5], an overview of several experimental methods in reference [34]. The experimental techniques also allowed the measurements of artificial atomic scale structures on surfaces [35, 36]. Of these measurements reference [35] investigates the interaction of two impurities on a surface. This is part of the inspiration for our excursus in chapter 4 and the calculations necessary as expanded upon in appendix chapter 8.1, as the directional component of such an interaction requires one to consider the structure of the surface. Experimentally the investigation of molecules on a surface has also been successfully demonstrated [37, 38, 39]. Reference [39] is here especially noteworthy in the context of this thesis, as it investigates chains in contact with a surface and the resulting effects on the properties of these chains. Inspired by this we will investigate trimer chains coupled to a surface and the required strength of such a coupling to induce certain changes in observables in the chapters 5 and 6. With respect to the experimental techniques mentioned above it is understandable that part of the recent theoretical work focuses on models enabling the description of a source and drain for electrons [40, 41, 42, 43, 44, 45, 46]. In our calculations in chapter 5 we use a single-channel model, while the two-channel approach in the excursus in chapter 4 is characterized by the two channels being part of the same surface as opposed to being a separate source and drain. Finally, in order to incorporate the outer magnetic field into the NRG calculations we use the same method also used by Höck for reference [47] and explained in full detail in reference [6].

2.4 Screening cloud and Kondo temperature

In the Kondo model the local moment of a magnetic impurity leads to a scattering of electrons and thus to the observed increase in resistance [7]. As we focus on the magnetic properties of the impurity it is however more important to us how the interaction of the impurity with the electrons affects the spin of the impurity and through it the magnetic observables. For the established picture of a spin $\frac{1}{2}$, a so called screening cloud should form below a threshold scale, the Kondo temperature, leading to a perfect screening at zero temperature [48]. Perfect screening means here that the impurity spin is effectively locked into a singlet state with the conduction band. The size of this screening cloud can be estimated as the Kondo coherence length ξ_K via:

$$\xi_K = \frac{\hbar v_F}{k_B T_K} \ , \tag{1}$$

with v_F the Fermi velocity. This length scale can reach mesoscopic values for typical values of v_F and T_K. Further investigations on the length scale and spatial correlations can be found in references [48, 28]. As the Kondo temperature, for references compare [49, 17, 6], is thus not only the scale at which the perturbation theory brakes down, but also defines the scale, below which a screening of an impurity could happen, it is useful to familiarize ourselves with it. Adapted for the context of the theory as presented in chapter 3 and thus the calculations in chapter 5 the scale of the Kondo temperature can be given by:

$$T_K = \sqrt{\frac{J_A}{W}} e^{-\frac{W}{J_A}} \frac{W}{k_B} \ . \tag{2}$$

For the most relevant scales to this thesis this relation between the Kondo temperature and the coupling of the impurity spin to a conduction electron can be visualized in figure 1.

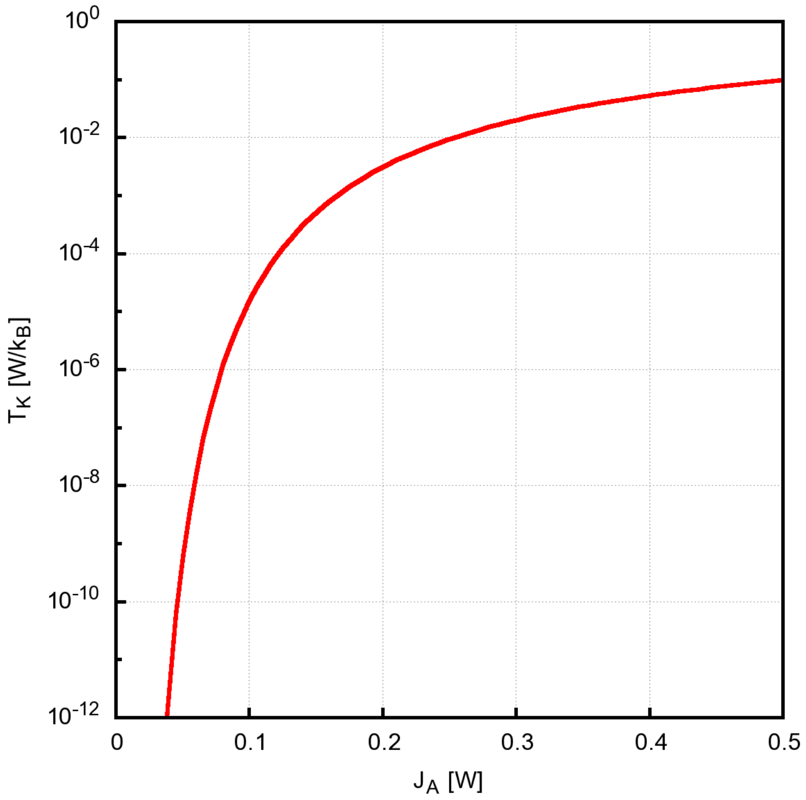

Figure 1: The Kondo temperature versus the coupling of the impurity to the conduction band.

For convenience the most relevant data points for the calculations in chapter 5 are listed in table 1.

$J_A[W]$	$T_K[W/k_B]$
0.06	$1.42 \cdot 10^{-8}$
0.15	$4.93 \cdot 10^{-4}$
0.2	$3.01 \cdot 10^{-3}$
0.5	$9.57 \cdot 10^{-2}$
1	$3.68 \cdot 10^{-1}$

Table 1: Values of the Kondo temperature for selected values of the coupling J_A of the impurity to the conduction band.

3 Theory

In this part of my thesis we will go into more details of the model and of the numerical solutions we implement to solve it. After we outlined our choice for the model to investigate in the previous chapter we will now look at this Hamiltonian and start with an overview to make the multi-step process to implement a solution more accessible. A lengthy discussion on the derivation of equations we use here has been done before and we direct all readers who require the full scope of those to reference [6], which is the basis for my implementation of the solution and which I personally proofread.

3.1 Overview

In the previous chapter we already concluded that our model should be of Kondo-type and consist of three parts representing the nonmagnetic metallic surface, the impurity and the interaction between those two. Our Hamiltonian may thus be written as:

$$\underset{\sim}{H} = \underset{\sim}{H}_{\text{electrons}} + \underset{\sim}{H}_{\text{coupling}} + \underset{\sim}{H}_{\text{impurity}} . \tag{3}$$

The first part $\underset{\sim}{H}_{\text{electrons}}$ represents non-interacting electrons on a lattice and is given by:

$$\underset{\sim}{H}_{\text{electrons}} = \sum_{i\neq j,\,\sigma} t_{ij} d^{\dagger}_{i\sigma} d_{j\sigma} + g\mu_B B \sum_{i} s^{z}_{i} . \tag{4}$$

The hopping parameter t_{ij} is non-zero only if the lattice sites i, j are nearest neighbors. $\underset{\sim}{d}^{\dagger}_{i\sigma}$ and $\underset{\sim}{d}_{j\sigma}$ are fermionic creation and annihilation operators for electrons with spin direction σ. The interaction with an external magnetic field B is given by the Zeeman term with $\underset{\sim}{s}^{z}_{i}$ representing the z-direction of the effective electron spin at lattice site i, g the g-factor and μ_B the Bohr magneton.

As we have already stated the following method can be applied to a wider variety of impurity and possibly coupling terms [6], but as we will choose specific parameters for our later calculations it is convenient to show a corresponding Hamiltonian here as illustrative representation:

$$\underset{\sim}{H}_{\text{impurity}} = 2\sum_{i<j} J_{ij} \underset{\sim}{\vec{S}}_{i} \cdot \underset{\sim}{\vec{S}}_{j} + g\mu_B B \sum_{i} \underset{\sim}{S}^{z}_{i} . \tag{5}$$

This part $\underset{\sim}{H}_{\text{impurity}}$ models the impurity, which depending on the experimental context could for example be a single molecule [38] or a chain of several of those [39]. These single spins or clusters thereof and their interactions are represented via an effective Heisenberg model for all connected spins $\underset{\sim}{\vec{S}}_i$ and via a Zeeman term. J_{ij} is the interaction between spins i and j and antiferromagnetic for a positive J_{ij}. With this effective spin model our last part of the Hamiltonian describes the interaction of these spins with a surface via:

$$\underset{\sim}{H}_{\text{coupling}} = 2 \cdot J_A \cdot \underset{\sim}{\vec{S}}_1 \cdot \underset{\sim}{\vec{s}}_0 \; . \tag{6}$$

The coupling constant J_A is positive for antiferromagnetic coupling. Other works may arbitrarily have chosen an alternative notation that features a coupling strength $J = 2J_A$. Furthermore it should be noted that this Hamiltonian can be easily expanded to include the interaction of multiple spins i of the cluster with the surface via:

$$\underset{\sim}{H}_{\text{coupling,exp}} = 2 \sum_i J_{A,i} \cdot \underset{\sim}{\vec{S}}_i \cdot \underset{\sim}{\vec{s}}_0 \; . \tag{7}$$

In both cases $\underset{\sim}{\vec{s}}_0$ represents the electron spin at the lattice site to which the impurity is coupled.

Starting here requires several steps of preparation before the problem can be treated numerically within the NRG method. We will present these steps in the following subsections, but give an overview here. First the Hamiltonian needs to be transformed to a continuous energy representation in the grand canonical ensemble and then be made dimensionless. Second with the electronic part of said Hamiltonian now including an integral with finite boundaries, it needs to be discretized for numerical treatment within the calculation while preserving its physical properties. Third to gain an easier numerical approach to the problem, it is tridiagonalized onto the so called Wilson chain. This is in fact a base transformation, for which parameters need to be obtained separately. Lastly this tridiagonalized form is then iteratively diagonalized and from those results thermodynamic observables can be obtained.

3.2 Transformation of the Hamiltonian

Starting from our model Hamiltonian we first transform the electron part in real space representation to a discrete momentum space representation. The result obtained is:

$$\utilde{H}_{\text{electrons}} = \sum_{\vec{k},\sigma} \epsilon_{\vec{k}} \utilde{c}^{\dagger}_{\vec{k}\sigma} \utilde{c}_{\vec{k}\sigma} + g\mu_B B \utilde{s}^{z}_{total} \, . \tag{8}$$

Here $\vec{k}$ is the momentum (quantum number), a vector, and $\epsilon_{\vec{k}}$ the dispersion relation assigning an energy to said momentum, while $\utilde{c}^{\dagger}_{\vec{k}\sigma}$ and $\utilde{c}_{\vec{k}\sigma}$ are the creation and annihilation operators for the electron states. It is important to note, that the information we want to incorporate into our calculations regarding the structure of the electronic lattice, that means the conduction band or the structure of the surface, is directly included here. After the transformation we then include the Zeeman term into the dispersion relation and account for the grand canonical ensemble by using the chemical potential, which is given by the Fermi-energy ϵ_F for our calculations. With the electronic part transformed we can adjust the interaction term of the Hamiltonian to fit the new description of the electrons (through $\utilde{\vec{s}}_0$ in $\utilde{H}_{\text{coupling}}$, see equation (6)) and end up with:

$$\utilde{H}_{\text{GC}} = \sum_{\vec{k},\sigma} (\epsilon_{\vec{k},\sigma} - \epsilon_F) \utilde{c}^{\dagger}_{\vec{k}\sigma} \utilde{c}_{\vec{k}\sigma} + \utilde{H}_{\text{coupling}} + \utilde{H}_{\text{impurity}} \, . \tag{9}$$

We can now treat this formulation of the Kondo model in the grand canonical ensemble with the NRG method. To this end we start by transforming the Hamiltonian to a continuous energy representation. This is achieved by letting the lattice size L on which the electrons are defined approach infinity. The now continuous representation includes an integral over the whole momentum space where we replace the dependency on the momentum by one on the energy using the dispersion relation mentioned above. This transformation has to ensure that the density of states $\rho(\epsilon)$ (per lattice site and per spin projection) is normalized, thereby including information about the dispersion relation into the new defined electron states via its definition:

$$\rho(\epsilon) = \frac{1}{L^d} \sum_{\vec{k}} \delta(\epsilon - \epsilon_{\vec{k}}) \ . \tag{10}$$

In our calculations we use the simplifying assumption of a constant density of states, that is widely used in other literature as well (compare e.g. ref. [23, 24, 25, 27, 43]), thus not capturing any special features of a lattice. Reference [6] shows how the density of states can be calculated for the simple case of one-dimensional tight-binding electrons. For the advanced task of capturing features of a two dimensional lattice, we expand on the calculations for a two dimensional square lattice in an excursus later on in chapter 4. We limit the energy range for which the problem is studied from negative to positive half-bandwidth. The half-bandwidth we further denote as W. Additionally in this transformation we retain only those electronic states which are also included in the interaction term, thus narrowing our potential focus to impurity properties, for which all relevant states are kept. Finally we bring the Hamiltonian to a "dimensionless representation" by rescaling with the half-bandwidth mentioned above. We furthermore split the integral into two parts to separate the positive from the negative spectrum of values. Again expressing the coupling part of the Hamiltonian appropriately via $\underset{\sim}{H}_{\text{coupling,NRG}}$ we arrive at:

$$\begin{aligned} \underset{\sim}{H}_{\text{NRG}} &= W \sum_{\mu} \Big(\frac{B_\mu^+}{W} \int_0^1 d\xi_\mu^+ \xi_\mu^+ \underset{\sim}{a}_\mu^{+\dagger}(\xi_\mu^+) \underset{\sim}{a}_\mu^+(\xi_\mu^+) + \frac{B_\mu^-}{W} \int_{-1}^0 d\xi_\mu^- \xi_\mu^- \underset{\sim}{a}_\mu^{-\dagger}(\xi_\mu^-) \underset{\sim}{a}_\mu^-(\xi_\mu^-) \Big) \\ &+ \underset{\sim}{H}_{\text{coupling,NRG}} + \underset{\sim}{H}_{\text{impurity}} \ . \end{aligned} \tag{11}$$

With similarity to the previous structure $\xi_\mu^\pm$ are "dimensionless energy values", to which the corresponding creation and annihilation operators are $\underset{\sim}{a}_\mu^{\pm\dagger}(\xi_\mu^\pm)$ and $\underset{\sim}{a}_\mu^{\pm}(\xi_\mu^\pm)$, while μ denotes the spin quantum number in z-direction. The dependence on the magnetic field is finally absorbed and the integrals correspondingly rescaled by:

$$B_\mu^\pm = | \pm W^\pm + \mu h| \ , \tag{12}$$

with h representing the magnetic field (times constants):

$$h = g\mu_B B \ , \tag{13}$$

and $W^{\pm}$ the half-bandwith shifted by the Fermi energy:

$$W^{\pm} = W \mp \epsilon_F \ . \tag{14}$$

For this representation h needs to be limited to the physically reasonable boundaries:

$$h < W^{\pm} \ . \tag{15}$$

A suitable representation for the coupling term is given by:

$$\underset{\sim}{H}_{\text{coupling,NRG}} = 2 \cdot J_A \cdot \underset{\sim}{\vec{S}} \cdot \sum_{\mu,\nu} \underset{\sim}{f}^{\dagger}_{0\mu} \frac{\vec{\sigma}_{\mu\nu}}{2} \underset{\sim}{f}_{0\nu} \ , \tag{16}$$

with $\vec{\sigma}_{\mu\nu}$ the vector of the Pauli matrices and $\underset{\sim}{f}_{0\mu}$ being defined as:

$$\begin{aligned} \underset{\sim}{f}_{0\mu} &= \int_0^1 d\xi_\mu^+ \sqrt{\rho(\xi_\mu^+ B_\mu^+ + \epsilon_F - \mu h) B_\mu^+} \, \underset{\sim}{a}_\mu^+(\xi_\mu^+) \\ &+ \int_{-1}^0 d\xi_\mu^- \sqrt{\rho(\xi_\mu^- B_\mu^- + \epsilon_F - \mu h) B_\mu^-} \, \underset{\sim}{a}_\mu^-(\xi_\mu^-) \ , \end{aligned} \tag{17}$$

and fulfilling standard anti-commutator relations.

3.3 Logarithmic discretization

The Hamiltonian we have obtained describes the conduction band via an integral effectively representing the continuous energy spectrum for the electrons. In order to treat it numerically this spectrum needs to be discretized. A linear discretization would require large numerical efforts to obtain results for lower temperatures. As we are, similar to the original treatments of the Kondo problem, interested in obtaining results for a wide range in temperature down to low energy scales, we use the logarithmic discretization as proposed by Wilson [17]. This discretization has the benefit of an increased resolution near the Fermi energy, which is at the center of our spectrum, i.e. the 0 boundary of our integrals. With those states being the most relevant to the lower energy physics this focus allows to cover a larger range of temperature for the same numerical cost in comparison to a linear mesh. Other forms of discretization might be possible, but the logarithmic discretization is additionally justified by the success of its results. Nevertheless, the form of discretization is an approximation to the continuous form of the problem and may thus result in numerical artifacts. To minimize those artifacts several improvements have been made to Wilson's original logarithmic discretization. One simple improvement can be made by averaging results for more than one mesh by slightly altering a parameter defining such a logarithmic mesh. This parameter is usually called the twist parameter z (introduced in ref. [22], naming e.g. ref. [25, 6]). Here we will now go over the basic idea of the logarithmic discretization with a twist parameter. The technical details of this and the improved versions can be found at reference [6]. For my calculations I used the optimal discretization by Zitko and Pruschke and averaged over two values of z (technical details in ref. [6], original ref. [25, 26]).

As discussed the logarithmic discretization aims at ever increasing accuracy at low energies near the Fermi energy for increasing numerical efforts. To this end the energy spectrum is divided into intervals. To define them we use two parameters. The first is Λ, the so-called discretization parameter, which is larger than 1. The second is the already introduced twist parameter z, which has to be larger than 0 but smaller than or equal to 1. For the calculations in this thesis I used Λ equal to 3. Furthermore it should be noted, that numerically the discretization needs to be carried out for each distinct kind of spin separately. In our case this means that spin up and spin down need to be treated separately for any non-zero magnetic field. On the basis of the two new parameters the starting intervals for the positive and negative energy spectrum respectively can be defined as:

$$\begin{aligned} I_0^+(z): &\quad \Lambda^{-z} &< \xi_\mu^+ \leq 1 \\ I_0^-(z): &\quad -1 &\leq \xi_\mu^- < -\Lambda^{-z}\ , \end{aligned} \tag{18}$$

while the m-th intervals are given by:

$$\begin{aligned} I_m^+(z): &\quad \Lambda^{-z-m} &< \xi_\mu^+ \leq \Lambda^{-z-m+1} \\ I_m^-(z): &\quad -\Lambda^{-z-m+1} &\leq \xi_\mu^- < -\Lambda^{-z-m}\ . \end{aligned} \tag{19}$$

Wilson's original discretization can be reproduced with z equal to 1. The corresponding intervals are displayed in graphic 2. Λ for this discretization, just as for my later calculations, is equal to 3.

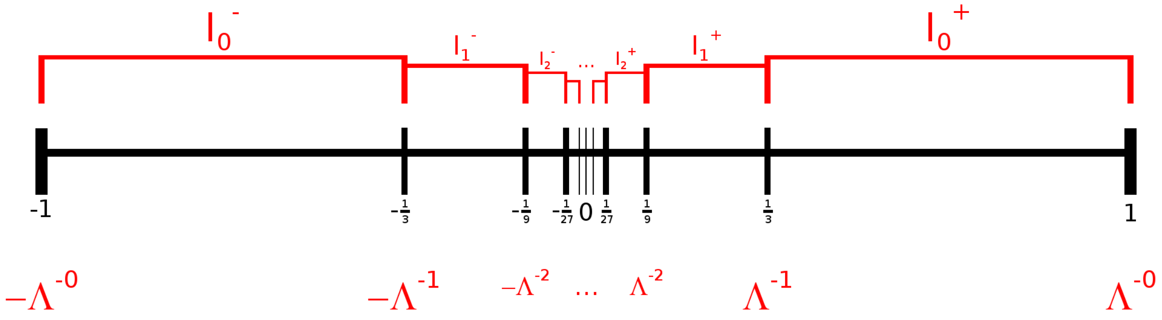

Figure 2: Sketch of the logarithmic discretization for $\Lambda = 3$.

The graphic allows to easily understand why the discretization is called logarithmic. In it every additional interval added to the discretization has its lower and upper boundary only at a third of the distance from 0 (the Fermi energy) compared to the respective boundaries of its predecessor. To achieve similar results for the lower boundaries, i.e. the boundaries closer to 0, in a linear discretization we would have to triple the amount of intervals in each step instead of adding just one interval. Due to the continuous nature of the energy band each interval itself is associated with an infinite amount of electronic states. We want to discretize their representation by selecting only one suitable state for each interval. To still be able to fully represent the interaction term with the impurity this state has to be constructed so that it is the only state that interacts with the impurity. This can be achieved by a proper projection within each interval. These states together thus allow an exact representation of the interaction term. One can now in principle construct a new basis for each interval starting with the selected state and represent the electronic term of the Hamiltonian with it. For a constant density of states this can be done by a Fourier expansion. In such a basis the electronic term however would not be diagonal anymore. The central approximation of the NRG is now to represent the conduction band and thus the electronic term not with this full basis but instead only with those states present in the reformulated interaction term, i.e. with those single states we previously selected for each interval. With this approximation we finally arrive at the discretized Hamiltonian:

$$\begin{aligned} \underset{\sim}{H}_{\text{NRG}} &\approx W \sum_{p,m,\mu} E^{p}_{m,\mu}(z)\, \underset{\sim}{a}^{p\dagger}_{m\mu}(z)\, \underset{\sim}{a}^{p}_{m\mu}(z) \\ &+ 2 \cdot J_A \cdot \underset{\sim}{S} \cdot \sum_{\mu,\nu} \underset{\sim}{f}^{\dagger}_{0\mu} \frac{\sigma_{\mu\nu}}{2} \underset{\sim}{f}_{0\nu} + \underset{\sim}{H}_{\text{impurity}} \; , \end{aligned} \tag{20}$$

with the interaction term represented by the same states $\underset{\sim}{a}^{p}_{m\mu}(z)$ as the electronic term via:

$$\underset{\sim}{f}^{\dagger}_{0\mu} = W \sum_{p,m} \sqrt{\frac{B^{p}_{\mu}}{W} W^{p}_{m,\mu}(z)}\, \underset{\sim}{a}^{p}_{m\mu}(z) \; . \tag{21}$$

m is again the interval in the discretization and p either plus or minus to indicate whether the positive or negative energy spectrum is referred to. This representation makes use of the weights:

$$W^p_{m\mu}(z) = \int_{I^p_m(z)} d\xi \rho(\xi B^p_\mu + \epsilon_F - \mu h) W \ , \tag{22}$$

for the interaction term. The dimensionless energy $E^p_{m\mu}(z)$ can be given as:

$$E^p_{m\mu}(z) = \frac{B^p_\mu}{W} \frac{\int_{I^p_m(z)} d\xi \xi \gamma^p_\mu(\xi)}{\int_{I^p_m(z)} d\zeta \gamma^p_\mu(\zeta)} \ . \tag{23}$$

However this is only the standard derivation and other choices are possible. This choice uses the weights:

$$\gamma^p_\mu(\xi) = \rho(\xi B^p_\mu + \epsilon_F - \mu h) B^p_\mu \ , \tag{24}$$

which can easily be traced back to equation (17) and thus the previously discussed projection onto the states in the interaction term. For more technical details I refer the reader again to [6].

3.4 Tridiagonalization

Our last representation of the Hamiltonian in equation (20) is discretized and divides the full spectrum of the conduction band into intervals. However the interaction term, as shown in equation (21), features an expansion in all these intervals and thus any truncation might directly affect results negatively. Therefore we introduce an additional base transformation that maps the problem onto a semi-infinite chain of electrons in a tight binding model with nearest neighbor interaction. The impurity constitutes the beginning and is then coupled to the state $\underset{\sim}{f}_{0\mu}$, which is commonly referred to as the zeroth chain site. The chain itself is called Wilson chain and is described by on-site energies $\epsilon_{n\mu}(z)$ and hopping parameters $t_{n\mu}(z)$. The base transformation is exact, but the parameters usually have to be determined numerically.

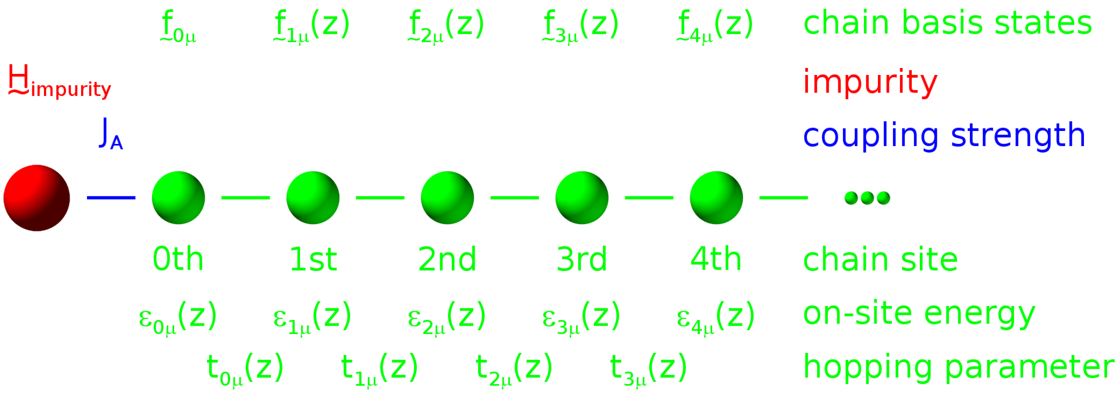

Figure 3: Sketch of the Wilson chain illustrating the relation between the chain basis states $\underset{\sim}{f}_{n\mu}$, the impurity Hamiltonian $\underset{\sim}{H}_{impurity}$, the coupling strength J_A, the on-site energies $\epsilon_{n\mu}(z)$, the hopping parameters $t_{n\mu}(z)$ and the chain sites.

The corresponding Hamiltonian is given by:

$$\begin{aligned} \underset{\sim}{H}_{\text{Wilson}}(z) &= \sum_{n=0,\mu}^{\infty} \Big[\epsilon_{n\mu}(z)\underset{\sim}{f}^{\dagger}_{n\mu}(z)\underset{\sim}{f}_{n\mu}(z) \\ &+ t_{n\mu}(z)(\underset{\sim}{f}^{\dagger}_{n\mu}(z)\underset{\sim}{f}_{n+1\mu}(z)) + \underset{\sim}{f}^{\dagger}_{n+1\mu}(z)\underset{\sim}{f}_{n\mu}(z))\Big] \\ &+ J\underset{\sim}{S}\cdot\sum_{\mu,\nu}\underset{\sim}{f}^{\dagger}_{0\mu}\frac{\sigma_{\mu\nu}}{2}\underset{\sim}{f}_{0\nu} + \underset{\sim}{H}_{\text{impurity}}\ . \end{aligned} \tag{25}$$

The basis states $\underset{\sim}{f}_{n\mu}(z)$ follow the canonical anti-commutation relation:

$$\{\underset{\sim}{f}_{n\mu}(z), \underset{\sim}{f}^{\dagger}_{n'\mu}(z)\} = \delta_{nn'}\delta_{\mu\nu} \; . \tag{26}$$

The on-site energies and hopping parameters can be derived via recursion relations. While I refer the reader again to [6] for the technical details, it is noteworthy that the recursive scheme requires high precision to be solved. The numerical solutions are usually unstable so that they will break down at some point. Thus all input prior to the scheme should best be analytical or given with arbitrary precision. The scheme itself is then carried out using arbitrary precision. In this thesis we calculate the parameters for 70 sites, though we may choose to not use all of them in an actual investigation (for their relation to the temperature range see chapter 3.5). When transforming the base via the recursion relation one has to choose a maximum number of intervals. In this thesis we use 2400. The chain can be viewed as tridiagonal for a single electron for a single spin projection. Once the parameters are calculated the problem is then solved by an iterative diagonalization procedure. Wilson for his original discretization found an analytical solution for the parameters. It can be used to test numerical code and shows the exponential decrease of the hopping parameters, that is characteristic for Wilson chains [17, 21, 6]:

$$\begin{aligned} \frac{\epsilon_n}{W} &= 0 \\ \frac{t_n}{W} &= \frac{1}{2}\frac{(1+\Lambda^{-1}(1-\Lambda^{-n-1})}{\sqrt{1-\Lambda^{-2n-1}}\sqrt{1-\Lambda^{-2n-3}}}\Lambda^{-\frac{n}{2}} && (27) \\ &\sim \Lambda^{-\frac{n}{2}}, n \gg 1, \textit{(asymptotical dependence in n)} \; . && (28) \end{aligned}$$

3.4.1 Iterative solution

The Wilson chain is semi-infinite and a numerical diagonalization can thus not treat it completely. The (Hilbert space) dimension of the problem for a given length n_{max} of the chain is:

$$D_{Wilson} = D_{Imp} 4^{n_{max}+1} \,, \tag{29}$$

where D_{Imp} is the dimension of the impurity and the chain length is counted after the zeroth site given by $\underset{\sim}{f}_{0\mu}$. In order to handle the problem for even larger chain sizes than can be treated directly, a special procedure is used called the iterative diagonalization. The idea is to diagonalize the Hamiltonian for a given size n and then cut states selected by criteria which preserve the physical properties of the chain before adding a new chain site and reiterating the procedure. Typically this procedure is only started after a certain chain size has been treated without cutting states. We, in this thesis, do not apply the cutting procedure for the first four chain sites after the zeroth site. To initialize the iterative diagonalization a start Hamiltonian has to be diagonalized. This usually consists of the impurity Hamiltonian and the zeroth lattice site. This Hamiltonian is diagonalized in order to obtain a first set of energy eigenvalues and corresponding states. When coupling the next chain site to it (and for every iteration thereafter) the obtained energy levels (of the previous step) split up. This splitting is of the order of magnitude of the hopping parameter assigned to the new chain site. This will usually also mean that the gap between the groundstate and the first excited state is of that order. As stated before the hopping parameter decreases along the Wilson chain exponentially. In order to keep the numbers suitable for numerical computation the groundstate in each step is set to zero and the Hamiltonian is rescaled so that the ground state gap is roughly of the order of one. One could in principle rescale with the hopping parameters directly, but as they can depend on the z-value (see previous chapter 3.4) this can complicate z-averaging needlessly. For this thesis we thus choose to rescale the Hamiltonian with the original analytical Wilson chain parameters as given in equation (27). We now have established, how we initialize the iterative diagonalization and how we rescale the Hamiltonian in each step. As stated above after a certain number of steps we start cutting some of the energy eigenvalues in order to keep the problem numerically solvable. Since we rescale the Hamiltonian and set the groundstate energy to zero, we can define a criterion for cutting states based on the energy value of a given state. For this thesis we want to discard all states with an energy higher than 20 (with no unit, due to rescaling of the Hamiltonian, see also (27) and (31)). We have to be careful however to not discard states that are part of a degeneracy, but due to small numerical errors are not easily recognized as such. Thus we introduce a minimum gap required between the state with highest energy that is kept and the one with the lowest energy that is discarded. For this gap we choose a value of 0.01. It should be noted that the numerical parameters are chosen by testing the robustness of calculations against a variation of them. Finally we note that the concept of discarding states with higher energy comes from the idea, that the hopping parameters and energies along the chain decrease exponentially. While the conduction electrons do not possess a characteristic energy scale in the original Hamiltonian, an artificial separation of energy scales is introduced via the logarithmic discretization.

3.5 Temperature

We now have established a procedure to calculate energy eigenvalues for different lengths of the Wilson chain by diagonalizing the chain iteratively. Next we want to calculate thermodynamic observables. We note that due to the nature of our procedure we have obtained sets of energy eigenvalues with a different spacing (i.e. different characteristic gap sizes between the lowest energy eigenvalues) for the different chain length we considered. The result is that appropriate temperatures can and must be assigned to the different length of the chain fragments calculated. Since we discarded higher energy eigenvalues during the iterative diagonalization we can now only consider temperatures sufficiently low so that the influence of those discarded states is neglectable. Additionally we have to remember that up to any chain length we diagonalize we only have considered spacings of a characteristic size or larger and that if we wanted to obtain physical properties resultant of smaller energy spacings we needed to continue the procedure for longer chain lengths first. Thus we can only assign temperatures that are sufficiently high, so that no details of smaller energy spacing need to be known. We note that due to the differences in actually calculating different observables these criteria will be fulfilled to a different degree by them, thus making the method more or less accurate for different observables. Since the problem and thus the eigenvalues are rescaled for every step as outlined above the problem of assigning a temperature is practically similar for every step. Given our information, that is the energy scale above which we discard states E'_{max}, which we chose to be 20, and the expected scale for the lowest excitation energies E'_{min}, which should be approximately 1 or lower, we thus must choose a new (rescaled) parameter β' to obtain the temperature according to the following equation:

$$E'_{min} \ll \beta'^{-1} \ll E'_{max} \ . \tag{30}$$

This (usually) results in values for β' between 0.1 and 1, but the quality of the final choice could depend on other parameters of the calculation. In this thesis we use three different values for β' in each step, 0.45, 0.5 and 0.55. This allows us not only to have a smoother curve by having more data points, but more importantly to have an indicator that the quality of the results is unaffected by the choice of the parameter. To calculate the actual temperature for the different chain length we have to undo the rescaling performed during the iterative diagonalization, so that we obtain β_N and thus the temperature. This can be done given the rescaling factor τ_{N-1}:

$$k_B T_N = \beta_N^{-1} = W \tau_{N-1} \beta'^{-1} \ , \tag{31}$$

and results in a temperature, which depends on the number of the step N in our iterative diagonalization. Since the rescaling factors decrease exponentially along the Wilson chain, the assigned temperatures for each step do so as well and the smallest temperature achievable for a given calculation is determined by the length of the chain itself.

3.6 Thermodynamic observables

Given the results of the previous sub chapters we can now calculate the thermodynamic observables. In order to do this, we use the eigenvalues and states obtained in each step of the iterative diagonalization to approximate the system for the corresponding temperatures in the grand canonical ensemble. As our previous approximations have focused on retaining the accuracy for the impurity properties and for its interaction with the conduction band, this is what we accordingly have to focus on in this chapter too. However the impurity and the conduction band are not weakly coupled, so that properties in general are not additive for the two subsystems and certain observables would not be well defined for a subsystem only. For those observables that we use in this thesis we are thus forced to consider two different concepts: the local observables, which can be well defined for the impurity subsystem alone, and the impurity contribution to an observable, which has to be calculated differently. We start with the latter.

3.6.1 Impurity contribution

As stated above we want to introduce the concept of the impurity contribution to an observable, so we can describe certain properties of the impurity system even if a thermodynamic observable can not be well defined for the impurity subsystem. Given an observable $O(T,B)$, we define the impurity contribution to that observable as:

$$O_{imp}(T,B) = O_{system\,with\,imp}(T,B) - O_{system\,without\,imp}(T,B)\ . \tag{32}$$

This definition allows us to calculate the impurity contribution by performing two separate calculations. A first calculation including the two subsystems impurity and conduction band and their interaction and a second calculation essentially only including the conduction band. Please note, that even if the observable can be calculated analytically for the conduction band it may be advisable to derive it numerically using the same method as for the complete system so that similar numerical errors may be eliminated when the difference is calculated for the impurity contribution [50, 6]. Furthermore while numerical differentiation is in principle possible other methods often achieve an acceptable accuracy more easily and are thus preferable. For this thesis we thus use the following equations:

$$Z = \sum_i e^{-\beta E_i}\ , \tag{33}$$

$$\frac{S}{k_B} = log(Z) + \frac{\beta}{Z}\sum_i E_i e^{-\beta E_i} \ , \tag{34}$$

with E_i the obtained energy eigenvalues, that are not discarded, Z the partition function and S the entropy. Within the considered model the total magnetization operator can be given by:

$$\underset{\sim}{M}_{tot} = -g\mu_B(\underset{\sim}{S}^z + \underset{\sim}{s}^z_{tot}) \ , \tag{35}$$

where $\underset{\sim}{S}^z$ is the z-direction of the total spin operator for the impurity subsystem and $\underset{\sim}{s}^z_{tot}$ the z-direction of the one for the conduction band. For this thesis we use the simplifying assumption that the g-factor is the same for the conduction electrons and the impurity spins. Since the total magnetization is a conserved quantity of the system [6], we can use eigenvalues $M_{tot,i}$ corresponding to the energy eigenvalues E_i to calculate the total magnetization:

$$M_{tot} = \frac{1}{Z}\sum_i M_{tot,i} e^{-\beta E_i} \ , \tag{36}$$

which we use to obtain the susceptibility χ times temperature:

$$\chi k_B T = \frac{1}{Z}\sum_i M^2_{tot,i} e^{-\beta E_i} - M^2_{tot} \ . \tag{37}$$

We note that to calculate the right hand side of all of these equations given above, it is irrelevant whether we use the rescaled values or not, as the factors cancel each other out in multiplications of β with E_i. However rescaled values are easier to handle numerically and are thus used in the actual computations. For the susceptibility this means that we consider susceptibility times temperature an observable, while the susceptibility alone is a derived quantity.

3.6.2 Local observables

In principle observables which can be well defined for the subsystem impurity can be calculated. However when a corresponding operator requires a matrix representation if they are not conserved quantities of the system, such a representation has to be transformed to a new basis for each step of the iterative diagonalization. This requires a non negligible amount of resources, thus the potential amount of considered local observables is limited for a single calculation. We will calculate the impurity magnetization as a local observable. Its operator is given as:

$$\underset{\sim}{M} = -g\mu_B \underset{\sim}{S}^z \ . \tag{38}$$

3.6.3 Averaging

As outlined in the previous sub chapter 3.3 we perform z-averaging in order to improve the numerical results. However, the truncated Wilson chain also displays even-odd differences in the observables. This effect can be reduced using an even-odd averaging. In this thesis we perform a linear interpolation according to the following formula [6]:

$$O_{e+o} = \frac{1}{2}\left[O(T_N) + O(T_{N-1}) + \frac{O(T_{N+1}) - O(T_{N-1})}{T_{N+1} - T_{N-1}}(T_N - T_{N-1})\right] \ . \tag{39}$$

This of course does not mix different temperatures that were assigned to the same step N of the iterative procedure but uses corresponding temperatures (i.e. those with the same value of β') from different steps. It should be noted that the z-averaging is performed after the even-odd averaging by:

$$O_{z-avg} = \frac{1}{n_Z}\sum_i O_{e+o}(z_i) \ , \tag{40}$$

with n_z the number of z-values used for the calculations, which is two for this thesis.

3.7 Unit system

In order to simplify the numerical calculations a special unit system is used. On the one hand this offers an advantage to the numerical calculations, while on the other hand it allows the results to depend on a freely choosable energy scale. In the following section an overview of this unit system is given. As the model of the system has already been introduced it is convenient to identify the choosable energy scale with the half-bandwidth W. Starting there other units can easily be chosen with respect to this scale. In the SI-System temperature, magnetic field and energy are independent units, but the respective quantities are connected within the physical equations. Thus choosing convenient units simplifies the actual calculations. Within the previously described model it is thus useful to choose the temperature scale W/k_B since the Boltzmann constant is used to connect energy and temperature scale. By the same logic $W/(g\mu_B)$ is chosen as the unit for the magnetic field. With these units chosen all others can be derived from the equations that are given by the model. This leads finally to the following units:

$$[E] = W \tag{41}$$

$$[B] = W/(g\mu_B) \tag{42}$$

$$[M] = g\mu_B \tag{43}$$

$$[T] = W/k_B \tag{44}$$

$$[\chi] = g^2 {\mu_B}^2/W \ . \tag{45}$$

These are sufficient to describe all results while retaining the freedom of choosing the energy scale W. If one desires to make the results more easily accessible with respect to known scales in the SI, one can choose to fix the scale W and express the previously described units in the SI or with respect to another non-SI units accepted for use with the SI. For pure convenience all units are listed with a conversion to the SI for the case that W is chosen to be $1eV$. This value is chosen as it might represent the right scale with respect to the expected systems (compare e.g. ref. [6, 51, 52]) and eV is a non-SI unit accepted for use with the SI. For g we assume a value of 2. However the original results are independent of such choices. The conversion is thus:

$$[E] = eV \tag{46}$$

$$[B] = eV/(g\mu_B) = 8.637993 \cdot 10^3 \cdot T \tag{47}$$

$$[M] = g\mu_B = 1.157676 \cdot 10^{-4} \cdot eV \cdot T^{-1} \tag{48}$$

$$[T] = eV/k_B = 1.160452 \cdot 10^4 \cdot K \tag{49}$$

$$[\chi] = g^2{\mu_B}^2/eV = 1.340214 \cdot 10^{-8} \cdot eV \cdot T^{-2}\ . \tag{50}$$

The conversion is based on the CODATA recommended values of the fundamental physical constants: 2014 [53] and results are rounded to 6 decimal places. This concludes the overview of the unit system.

4 Excursus: Normalization factors in the two impurity two dimensional (square) lattice Kondo model

In the previous chapter we have outlined the preparatory work and theory necessary for NRG calculations on a one dimensional, practically featureless lattice. That is all that is necessary in order to perform and understand the later chapter on calculations. This chapter is an excursus building on the foundations laid out in the chapter on theory and explaining some of the groundwork required in order to expand calculations, so that they include the features of the underlying lattice, in particular those of a two dimensional (square) lattice[1]. Such an approach is especially interesting when looking at multiple impurities that are coupled to the lattice in relative proximity, so that they may indirectly be interacting with one another. In that case the underlying structure of the lattice can influence such an interaction. Experimentally a similar scenario is featured in reference [35]. In relation to the structure of the previous chapter a suitable starting point would again be a local representation of the Hamiltonian like the one in chapter 3.1, outlined by the formulas (3), (4), (5) and (6), with hopping parameters changed to describe nearest neighbor hopping on a two dimensional square lattice and featuring interactions for two impurities as well as coupling those to two different lattice sites.

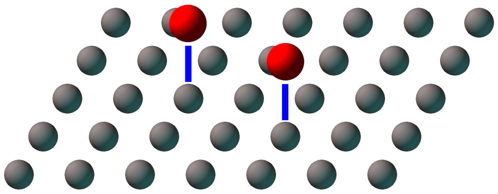

Figure 4: Sketch of two impurities (red) above a section of a square lattice (grey) connected (blue) to two different lattice places. The full lattice extends indefinitely.

Analogous to our discussion in chapter 3.2 our first step then is to transform the Hamiltonian from local space to a discrete momentum space. By doing so, the description of the lattice structure as given by the hopping parameters is incorporated into the disper-

---

[1] This expansion on the previous theory chapter is based on notes of and discussions with Dr. Höck. Early use of even/odd splitting in the context can be found for example in the references [54, 55].

sion relation. With two orthogonal axis in the lattice, we can give the dispersion relation by extending the solution given for the one dimensional case in reference [6], so that we get:

$$\epsilon_{\vec{k}} = -2t[cos(k_1) + cos(k_2)] \ . \tag{51}$$

Here k_1 and k_2 are the momenta in the two orthogonal directions of the lattice, ranging in value between $[-\pi, \pi)$. On this basis we can calculate the density of states following our outline in formula (10). This time we do not want to make the simplifying assumption of a constant density of states. The actual calculation is done in continuous momentum space and yields:

$$\rho(\epsilon) = \frac{1}{2 \cdot \pi^2 t} K\left(\tilde{m} = \tilde{k}^2 = [1 - \frac{\epsilon^2}{16 \cdot t^2}]\right) \ , \tag{52}$$

where $K(\tilde{m} = \tilde{k}^2)$ is the complete elliptic integral of the first kind (which depending on the source is sometimes defined via $\tilde{m}$ or $\tilde{k}$, with $\tilde{m} = \tilde{k}^2$) and t the nearest neighbor hopping parameter. Reference [56] allows us to verify that (taking into account differing definitions of variables and the definition of the elliptic integral). In the previously discussed simpler case of a single impurity, we continued from here (with a constant density of states) to a continuous momentum space representation and then an energy representation before starting the standard NRG approach. In this chapter however we do not have a single impurity, but work with two. This means as we transform from a local to a momentum space representation we have to consider our definition of the effective electron spin at our first lattice site more closely, as it is linked to the spin at the site where we place our second impurity. A suitable representation for the electron spin at a lattice site $\vec{R}$ is given by:

$$\vec{s}_{mom}(\vec{R}) = \frac{1}{2L^2} \sum_{\vec{k},\vec{k'},\mu,\nu} e^{i2\pi \frac{\vec{k'}-\vec{k}}{L} \cdot \vec{R}} \underset{\sim}{c}^{\dagger}_{\vec{k}\mu} \vec{\sigma}_{\mu\nu} \underset{\sim}{c}_{\vec{k'}\nu} \ . \tag{53}$$

For the case of a single impurity one is able to set the lattice site $\vec{R}$ equal to the origin of the coordinate system. Since we have now two impurities the phase factor can not be eliminated in this way. Nonetheless, we can still center our coordinate system on one impurity so that $\vec{R}$ describes the distance to the other one. Furthermore we will be assuming that $\vec{R}$ gives the distance in form of integers counting the distance in lattice sites along the natural axis of the lattice given by the nearest neighbors to any site. Lastly we transform the basis by a factor to the basis of $e^{-i\vec{k}\vec{R}/2}$. With this we can now describe the system in continuous momentum space representation via the Hamiltonian:

$$\begin{aligned} \underset{\sim}{H}_{2I} &= H_{imp} + \sum_{\sigma} \int d\vec{k}\epsilon_\sigma(\vec{k}) \underset{\sim}{a}^\dagger_{\vec{k}\sigma}\underset{\sim}{a}_{\vec{k}\sigma} \\ &+ \frac{1}{8\pi^2}\sum_{\mu,\nu}\int d\vec{k}\int d\vec{k}' \underset{\sim}{a}^\dagger_{\vec{k}\mu}\vec{\sigma}_{\mu\nu}\underset{\sim}{a}_{\vec{k}'\nu}[J_1\vec{S}_1 e^{i(\vec{k}'-\vec{k})\cdot\vec{R}/2} + J_2\vec{S}_2 e^{-i(\vec{k}'-\vec{k})\cdot\vec{R}/2}]\,, \end{aligned} \tag{54}$$

with $\underset{\sim}{a}^\dagger_{\vec{k}\sigma}$ and $\underset{\sim}{a}_{\vec{k}\sigma}$ the creation and annihilation operators for the electron states.

This Hamiltonian as in the simpler case before has to be transformed to an energy space representation. To this end we define the following transformations:

$$\underset{\sim}{a}_{\epsilon,+,\sigma} = \int d\vec{k}\delta(\epsilon - \epsilon(\vec{k}))e^{i\vec{k}\cdot\vec{R}/2}\underset{\sim}{a}_{\vec{k},\sigma} \tag{55}$$

$$\underset{\sim}{a}_{\epsilon,-,\sigma} = \int d\vec{k}\delta(\epsilon - \epsilon(\vec{k}))e^{-i\vec{k}\cdot\vec{R}/2}\underset{\sim}{a}_{\vec{k},\sigma}\,, \tag{56}$$

which we use in turn to arrive at:

$$\underset{\sim}{a}_{\epsilon,e,\sigma} = \frac{1}{N_e(\epsilon)}[\underset{\sim}{a}_{\epsilon,+,\sigma} + \underset{\sim}{a}_{\epsilon,-,\sigma}] \tag{57}$$

$$\underset{\sim}{a}_{\epsilon,o,\sigma} = \frac{1}{N_o(\epsilon)}[\underset{\sim}{a}_{\epsilon,+,\sigma} - \underset{\sim}{a}_{\epsilon,-,\sigma}]\,, \tag{58}$$

Here $N_e(\epsilon)$ and $N_o(\epsilon)$ are the two normalization factors, which will be important later. With this basis the Hamiltonian can be written in an energy representation:

$$\begin{aligned}
\underset{\sim}{H}_{En} &= H_{imp} + \sum_{\sigma} \int d\epsilon(\epsilon + \sigma g \mu_B)(\underset{\sim}{a}^{\dagger}_{\epsilon,e,\sigma}\underset{\sim}{a}_{\epsilon,e,\sigma} + \underset{\sim}{a}^{\dagger}_{\epsilon,o,\sigma}\underset{\sim}{a}_{\epsilon,o,\sigma}) \\
&+ \frac{1}{32\pi^2}\sum_{\mu,\nu}(J_1\vec{S}_1 + J_2\vec{S}_2)[f^{\dagger}_{e,\mu}\vec{\sigma}_{\mu\nu}f_{e,\nu} + f^{\dagger}_{o,\mu}\vec{\sigma}_{\mu\nu}f_{o,\nu}] \\
&+ \frac{1}{32\pi^2}\sum_{\mu,\nu}(J_1\vec{S}_1 - J_2\vec{S}_2)[f^{\dagger}_{e,\mu}\vec{\sigma}_{\mu\nu}f_{o,\nu} + f^{\dagger}_{o,\mu}\vec{\sigma}_{\mu\nu}f_{e,\nu}] \ , \qquad (59)
\end{aligned}$$

with the zeroth site function:

$$\begin{aligned}
\underset{\sim}{f}_{e,\sigma} &= \int d\epsilon N_e(\epsilon)\underset{\sim}{a}_{\epsilon,e,\sigma} \qquad (60) \\
\underset{\sim}{f}_{o,\sigma} &= \int d\epsilon N_o(\epsilon)\underset{\sim}{a}_{\epsilon,o,\sigma} \ . \qquad (61)
\end{aligned}$$

The energy integration should here be restricted similarly as to the one dimensional case. In the Hamiltonian the first sum representing the conduction electron part now includes two terms, so that the electrons can be mapped to two different chains as a result of the even-odd splitting. Structurally the rest can be handled as in the simpler case before. However numerically since we did not use the simplification of a constant density of states the normalization factors $N_e(\epsilon)$ and $N_o(\epsilon)$ require additional work:

$$\begin{aligned}
N_e^2(\epsilon) &= 4\int d\vec{k}\delta(\epsilon - \epsilon(\vec{k}))\cos^2(\vec{k}\cdot\vec{R}/2) \qquad (62) \\
N_o^2(\epsilon) &= 4\int d\vec{k}\delta(\epsilon - \epsilon(\vec{k}))\sin^2(\vec{k}\cdot\vec{R}/2) \ . \qquad (63)
\end{aligned}$$

We see that the normalization factors consist of an integral similar to the density of states but have an additional factor in the trigonometrical functions. As we have outlined in the chapter on tridiagonalization it is important that we can obtain all parameters prior to that to arbitrary precision with reasonable numerical effort. As it turns out the representation of the density of states via the complete elliptic integral of the first kind satisfies that condition. For the normalization factor it is now necessary to obtain such a representation as well. I was unable to find a *general* solution to these factors, nevertheless a suitable representation can be found for fixed values of $\vec{R}$, the difference vector between the coupling sites of the two impurities. The systematic as well as examples can be found in the appendix chapter 8.1.

5 Calculations

After the introduction to the theory behind the NRG calculations we now want to use this method to obtain numerical results for a couple of interesting systems. A system of two spins $\frac{1}{2}$, a dimer, is the easiest option to include internal interactions. Adding an additional spin $\frac{1}{2}$, so that we obtain a trimer, allows us further to introduce an internal structure to the system by choosing which of the three spins are internally coupled. Since our motivation behind this is to understand how the properties of free systems, that we already can describe well, change due to contact with a nonmagnetic metallic surface, we start this chapter with a short summary of properties for a free dimer and free trimer chain that will help us in the following discussions.

5.1 Free dimer and trimer chain systems

As the properties of the free systems are well understood, this paragraph will be short and serves merely to give the reader context. We describe the free dimer and trimer chain system with the following Hamiltonian:

$$\begin{aligned} \underset{\sim}{H}_{\text{fDimer}} &= 2J_I \underset{\sim}{\vec{S}}_1 \cdot \underset{\sim}{\vec{S}}_2 + g\mu_B B \sum_i \underset{\sim}{S}_i^z & (64) \\ \underset{\sim}{H}_{\text{fTrimerC}} &= 2J_I (\underset{\sim}{\vec{S}}_1 \cdot \underset{\sim}{\vec{S}}_2 + \underset{\sim}{\vec{S}}_2 \cdot \underset{\sim}{\vec{S}}_3) + g\mu_B B \sum_i \underset{\sim}{S}_i^z \ . & (65) \end{aligned}$$

These are specialty cases of the same Hamiltonian that we introduced in equation (5) to describe an impurity. Since the latter part of the Hamiltonian, the Zeeman term, commutes with the former part, the Heisenberg term, we may solve only the Heisenberg term to obtain the energy eigenvalues and then adjust them as needed for a non-zero magnetic field. The problem is analytically solvable [57] and we can obtain a solution for our systems by completing the square. From the spin degrees of freedom we know that the dimer system features four states, while the trimer features eight. Figure 5 shows a sketch of the energy eigenvalues and their dependence on the magnetic field. Similarly to the trimer chain results can also be obtained for different structures of a trimer.

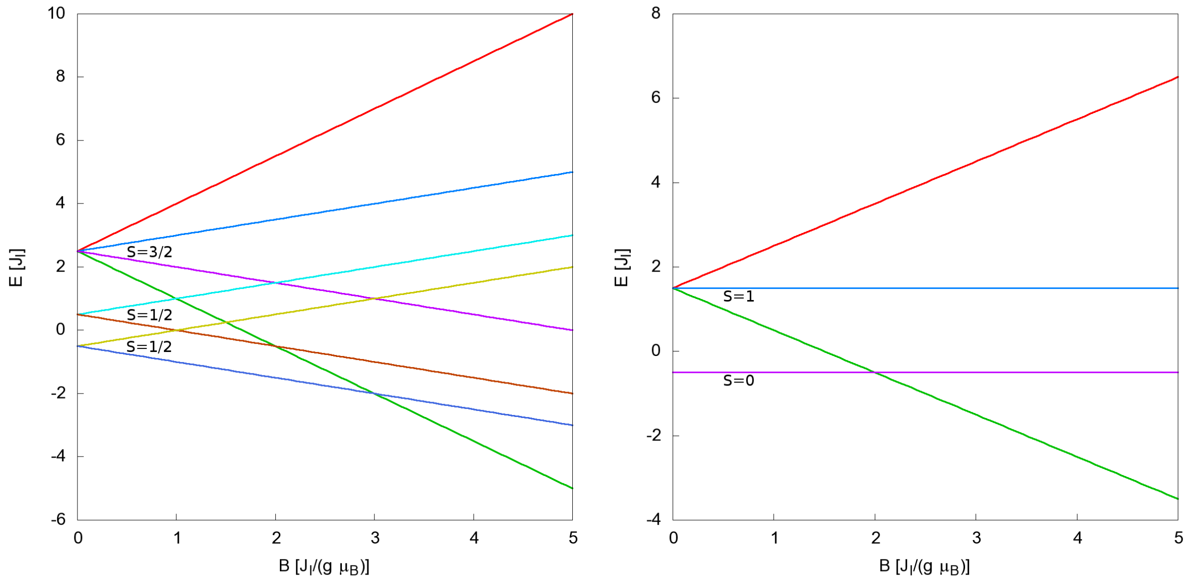

Figure 5: Sketch of the energy eigenvalues and their depence on the magnetic field for a free trimer chain (left) and a free dimer (right). S is the total spin of the system.

5.2 (Doubly coupled) dimer system

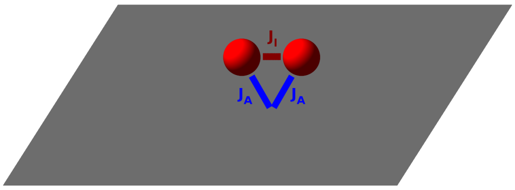

Figure 6: Sketch of a dimer impurity (red) above a section of a lattice (grey) connected (blue) to the same lattice site. The full lattice extends indefinitely.

This chapter will present results for a simple dimer system and serves as an introduction. Dimer systems have been treated before, most notably in references [58, 59]. Using our general Hamilton operator (3), we choose the impurity part of it to match the Hamiltonian of the free dimer we just introduced in (64). Furthermore we choose both spins within the impurity to couple to the substrate. The Hamiltonian thus is:

$$\begin{aligned} \underset{\sim}{H} &= \underset{\sim}{H}_{\text{electrons}} + \underset{\sim}{H}_{\text{coupling}} + \underset{\sim}{H}_{\text{impurity}} \\ \underset{\sim}{H}_{\text{impurity}} &= 2J_I \underset{\sim}{\vec{S}}_1 \cdot \underset{\sim}{\vec{S}}_2 + g\mu_B B \sum_i \underset{\sim}{S}_i^z \\ \underset{\sim}{H}_{\text{coupling}} &= 2\sum_i J_A \cdot \underset{\sim}{\vec{S}}_i \cdot \underset{\sim}{\vec{s}}_0 \; . \end{aligned} \tag{66}$$

We choose the intra-impurity coupling to be antiferromagnetic. Both spins are connected to the conduction band via the same coupling strength J_A. Our focus in this chapter will be the two observables (impurity contribution to the) entropy and (impurity contribution to the) susceptibility times temperature and their behavior versus the temperature on a logarithmic scale. Using two spins $s = \frac{1}{2}$ we know that the free dimer spin system has four states. We thus expect the (impurity contribution to the) entropy for the complete system to be between $ln4$ and $ln1 = 0$. In the following we label the system with $J_A = 0$ the free system. The impurity contribution to an observable for the free system should behave as if no conduction band was present, i.e. as if it was the actual observable for the uncoupled spin system alone. We thus expect the impurity contribution for the entropy for the free dimer to drop from $ln4$ to $ln1$ at a temperature scale corresponding to the intra-impurity coupling, which we set to $5 \cdot 10^{-2}$. In figure 7 we observe that this is indeed the case (red squares).

If we now increase the coupling to the conduction band, this introduces a new temperature scale, the aforementioned Kondo temperature, to the system. For the second graph (green circles) within figure 7 we increase J_A to $0.2W$ and observe that the graph is qualitatively similar to that of the free dimer (red squares), but drops to $ln1$ at a lower temperature. To understand this we remind ourselves that the coupling J_A is antiferromagnetic and that both spins of the impurity dimer are coupled to the conduction band at a single electron site. This, which may be seen as similar to the RKKY interaction [58], results in an effective indirect ferromagnetic coupling of the dimer spins competing with the antiferromagnetic intra-impurity coupling J_I and thus lowering the temperature scale at which intra-impurity states freeze out. For the third graph (blue diamonds) in figure 7 we now lower the intra-impurity coupling to $J_I = 0.007W$, which results in the graph heading to $ln2$ for low temperatures. This is the first graph where we observe screening of impurity spins by the conduction electron leaving the impurity

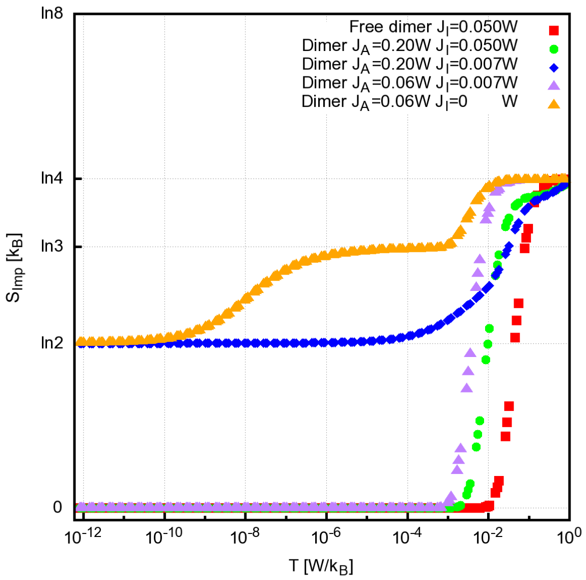

Figure 7: Impurity contribution to the entropy vs. temperature for different parameter choices of a (doubly coupled) dimer system. Beginning at the top of the key and going down, the first graph (red squares) shows a free dimer with intra-impurity coupling $J_I = 0.05W$. The second graph (green circles) features the same intra-impurity coupling of $J_I = 0.05W$, but includes a coupling to the conduction band with $J_A = 0.2W$. The third graph (blue diamonds) is based on a variation of the intra-impurity coupling to $J_I = 0.007W$, while using the same strength for the coupling to the conduction band of $J_A = 0.2W$. The fourth graph (purple triangles) features a weaker coupling to the conduction band with $J_A = 0.06W$ and an intra-impurity coupling of $J_I = 0.007W$. For the fifth and last graph (orange triangles) the coupling to the conduction band is again set to $J_A = 0.06W$, while no intra-impurity coupling is present.

system with an effective spin $\frac{1}{2}$, which we will later confirm by looking at (the impurity contribution to) the susceptibility times temperature. For the fourth graph (purple triangles) in figure 7 we now lower the coupling J_A to $0.06W$, thus lowering the Kondo temperature as well and return to a dominance of the intra-impurity coupling and a qualitatively similar behavior to the free dimer. Finally for the fifth and last graph (orange triangles) within figure 7 we set the intra-impurity coupling J_I to 0. This leads to the graph heading to $ln2$ at low temperatures since the intra-impurity coupling can no longer lead to a freezing out of impurity degrees of freedom, but at intermediate temperatures the graph plateaus at $ln3$. The reason for this is that, due to the lack of intra-impurity coupling J_I, the indirect ferromagnetic interaction between the two dimer spins via the conduction band dominates this intermediate temperature scale and energetically separates the single antiferromagnetic dimer state from the other three.

To confirm our reasoning regarding the graphs in figure 7 we now look at figure 8, where (the impurity contribution to) the susceptibility times temperature is plotted against the temperature. The values for the different couplings are the same as in figure 7. For the graph of the free dimer (red squares) and the two graphs (green circles, purple triangles) that behave similar to it we see a value of approximately $0.5(g\mu_B)^2/k_B$ at high temperatures and a drop to 0 for low temperatures. The graphs that are dominated by the Kondo screening at low temperatures (blue diamonds, orange triangles) in contrast head to $0.25(g\mu_B)^2/k_B$, while showing the same value of $0.5(g\mu_B)^2/k_B$ at high temperatures. Both of them also show a bump at intermediate temperatures, which however is only pronounced in the last of the graphs (orange triangles) and reaches a value of approximately $\frac{2}{3}(g\mu_B)^2/k_B$. With the formula from reference [60]:

$$T\chi = const. = \frac{1}{3}S(S+1)(g\mu_B)^2/k_B \ , \tag{67}$$

where S is a spin, we can associate the values observed with states of the impurity system. A value of $0.5(g\mu_B)^2/k_B$ at high temperatures is the result of two (practically free) spins $\frac{1}{2}$ each contributing $0.25(g\mu_B)^2/k_B$ to the sum. A value of 0 signals a total spin of 0 for the impurity, which is the ground state for two antiferromagnetically coupled spins $\frac{1}{2}$. This supports our interpretation of figure 7 regarding the graphs similar to the free dimer (green circles, purple triangles) since the other impurity degrees of freedom are frozen out. For the graphs heading to a value of $0.25(g\mu_B)^2/k_B$ (blue diamonds, orange triangles) in figure 8, we can associate a spin $\frac{1}{2}$ system, which supports the reasoning that a spin $\frac{1}{2}$ of the dimer system is screened by the conduction electrons thus leaving a $\frac{1}{2}$ system behind. Finally the pronounced bump at intermediate temperatures for the last graph (orange triangles) of figure 8 and the value $\frac{2}{3}(g\mu_B)^2/k_B$ corresponds to a total spin 1, thus supporting our interpretation of figure 7 that an indirect ferromagnetic coupling is responsible for the behavior of the graph (orange triangles) at intermediate temperatures.

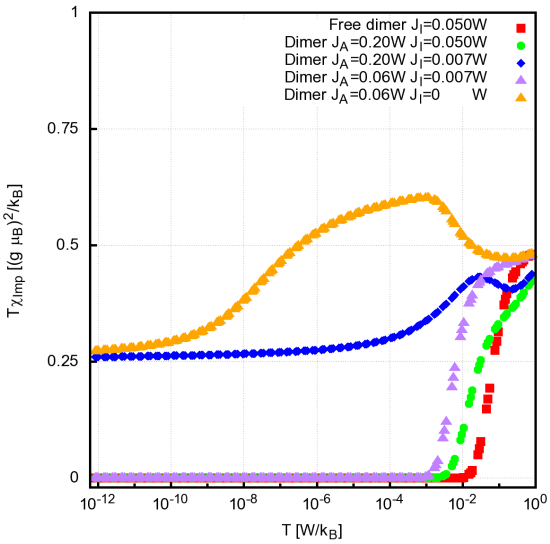

Figure 8: Impurity contribution to the susceptibility times temperature vs. temperature for different parameter choices of a (doubly coupled) dimer system. Beginning at the top of the key and going down, the first graph (red squares) shows a free dimer with intra-impurity coupling $J_I = 0.05W$. The second graph (green circles) features the same intra-impurity coupling of $J_I = 0.05W$, but includes a coupling to the conduction band with $J_A = 0.2W$. The third graph (blue diamonds) is based on a variation of the intra-impurity coupling to $J_I = 0.007W$, while using the same strength for the coupling to the conduction band of $J_A = 0.2W$. The fourth graph (purple triangles) features a weaker coupling to the conduction band with $J_A = 0.06W$ and an intra-impurity coupling of $J_I = 0.007W$. For the fifth and last graph (orange triangles) the coupling to the conduction band is again set to $J_A = 0.06W$, while no intra-impurity coupling is present.

5.3 (Triply coupled) trimer system

After we have completed our analysis of the results for the dimer we now add an additional spin $\frac{1}{2}$, which is coupled antiferromagnetically to both spins of the dimer and to the conduction band. We choose the couplings so that the result is a symmetrical three spin ring, to which we may refer to as triangle. Triangular shapes in the context of the Kondo problem have been investigated before, for example in references [42, 45, 61].

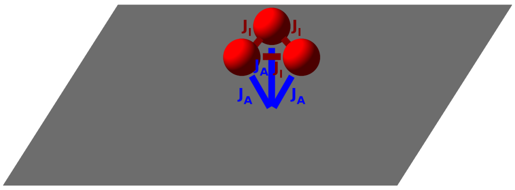

Figure 9: Sketch of a symmetrical trimer impurity (red) above a section of a lattice (grey) connected (blue) to the same lattice site. The full lattice extends indefinitely.

For the impurity this means, that we move from the four original states of the dimer to eight states in the trimer. As depicted in figure 5 of chapter 5.1 the original four states of the dimer were total spin 0, M quantum number 0 ("antiferromagnetically aligned") and total spin 1 ("ferromagnetically aligned"), M quantum numbers -1,0,1. Adding a spin $\frac{1}{2}$ for the (trimer) triangle, we get four antiferromagnetically aligned states, total spin $\frac{1}{2}$, M quantum numbers -$\frac{1}{2}$, $\frac{1}{2}$ each twofold degenerate, and four ferromagnetically aligned states, total spin $\frac{3}{2}$, M quantum numbers -$\frac{3}{2}$, -$\frac{1}{2}$, $\frac{1}{2}$, $\frac{3}{2}$.

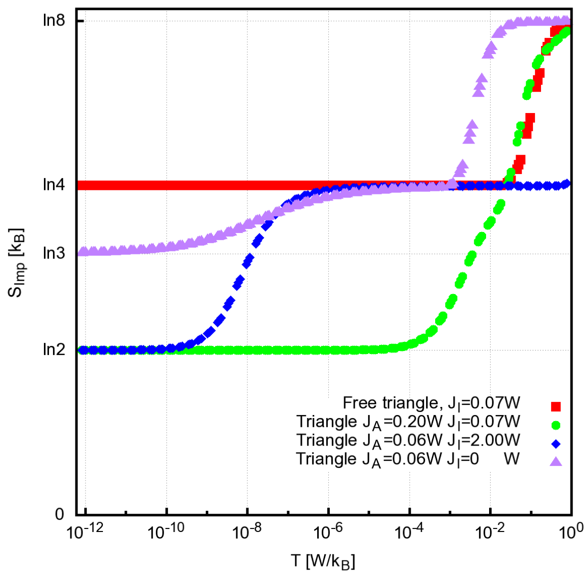

Figure 10: Impurity contribution to the entropy vs. temperature for different parameter choices of a (triply coupled) trimer system. Beginning at the top of the key and going down, the first graph (red squares) shows a free triangle with intra-impurity coupling $J_I = 0.07W$. The second graph (green circles) features the same intra-impurity coupling of $J_I = 0.07W$, but includes a coupling to the conduction band with $J_A = 0.2W$. For the third graph (blue diamonds) the intra-impurity coupling is set to $J_I = 2W$ and the coupling to the conduction band is set to $J_A = 0.06W$. The fourth and last graph (purple triangles) features the same coupling to the conduction band with $J_A = 0.06W$, while no intra-impurity coupling is present.

With these states in mind we examine the first graph (red squares) of figure 10. The free (trimer) triangle shows a drop from $ln8$ to $ln4$ at high temperatures. Since no interaction with a conduction band is present and the spins are antiferromagnetically coupled we attribute this drop to a freezing out of the four ferromagnetically aligned states. Referencing figure 11, which shows the (impurity contribution to the) susceptibility times temperature, we confirm that only states with spin $\frac{1}{2}$ remain. For the second graph (green circles) in figure 10 we now increase the coupling to the conduction band. At a similar temperature to the first graph (red squares) we see an almost seamless drop from $ln8$ to $ln2$. Referencing figure 11 we note that there is still a drop similar to the free triangle at first. After that follows a drop to 0. We conclude thus that a freezing out of ferromagnetically aligned states happens and is directly followed by or transitions into a screening of a spin $\frac{1}{2}$. This leads to a remaining spin 0, which is still twofold degenerate. For the third graph (blue diamonds) we separate the temperature scales for freezing out and screening and observe the qualitatively same behavior as in the second graph (green circles). Finally for the fourth graph (purple triangles) we set the intra-impurity coupling zero. The indirect ferromagnetic coupling induced by the coupling to the conduction band leads to a freezing out of the antiferromagnetically aligned states, so that at intermediate temperatures the four ferromagnetically aligned states remain. The coupling to the conduction band now leads to these spin $\frac{3}{2}$ states being screened to spin 1 and thus leaves 3 states remaining at low temperatures. We confirm this by referencing the fourth graph (purple triangles) in figure 11, which shows an increase to almost $1.25(g\mu_B)^2/k_B$, which is associated with spin $\frac{3}{2}$, followed by a drop heading to $\frac{2}{3}(g\mu_B)^2/k_B$, which can be attributed to spin 1.

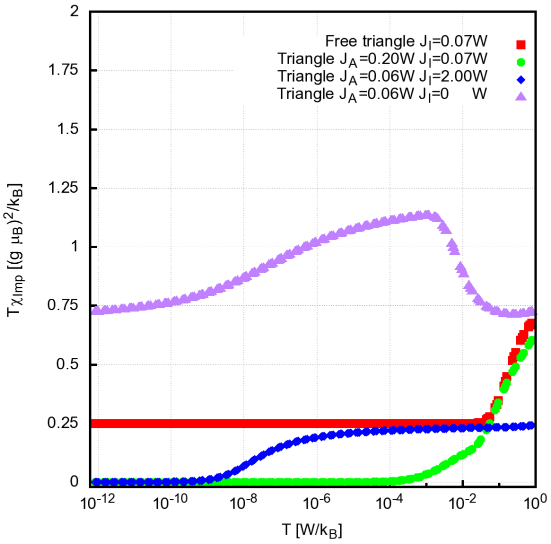

Figure 11: Impurity contribution to the susceptibility times temperature vs. temperature for different parameter choices of a (triply coupled) trimer system. Beginning at the top of the key and going down, the first graph (red squares) shows a free triangle with intra-impurity coupling $J_I = 0.07W$. The second graph (green circles) features the same intra-impurity coupling of $J_I = 0.07W$, but includes a coupling to the conduction band with $J_A = 0.2W$. For the third graph (blue diamonds) the intra-impurity coupling is set to $J_I = 2W$ and the coupling to the conduction band is set to $J_A = 0.06W$. The fourth and last graph (purple triangles) features the same coupling to the conduction band with $J_A = 0.06W$, while no intra-impurity coupling is present.

5.4 Trimer dimer transitions

For this calculation we draw our inspiration from one of the experiments mentioned in the introduction in chapter 2. Chen et al. [39] managed to stack Cobalt phthalocyanine (CoPc) molecules in layers on top each other with a lead (Pb) substrate underneath. The molecules contain a single Co^{2+}, so that they effectively feature a single spin $\frac{1}{2}$ as a magnetic center. In the experiment these molecules interacted with each other and were stacked so that spin chains were formed. Chen et al. now studied the spectrum of these chains and also observed the Kondo effect.
With this effective creation of spin chains in mind we want to investigate the effect of the strength of the impurity-surface interaction by observing the change of the groundstate for the system in an external magnetic field. Since a trimer chain would still leave us a dimer and thus an internal interaction even if a single spin is fully screened, it is the shortest chain to consider. Our model thus consists of three spins $\frac{1}{2}$ forming a chain, where only one spin interacts directly with the conduction band.

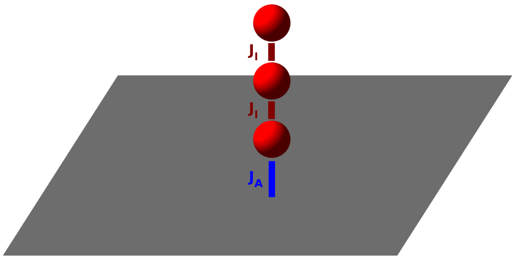

Figure 12: Sketch of a trimer chain impurity (red) above a section of a lattice (grey) singly connected (blue) to a single lattice site. The full lattice extends indefinitely.

Due to our motivation our focus is on the (impurity) magnetization versus the external magnetic field as our main observable. In this context we will use the term crossing field, which is the strength of the external magnetic field, that needs to be applied to induce a transition in the groundstate of a system. Since we already treated the free dimer and trimer chain in chapter 5.1, we can easily depict the energy eigenvalues and the crossing fields for them. Figure 13 shows the Zeeman levels and the clear dependence of the crossing fields on the intra-impurity coupling.

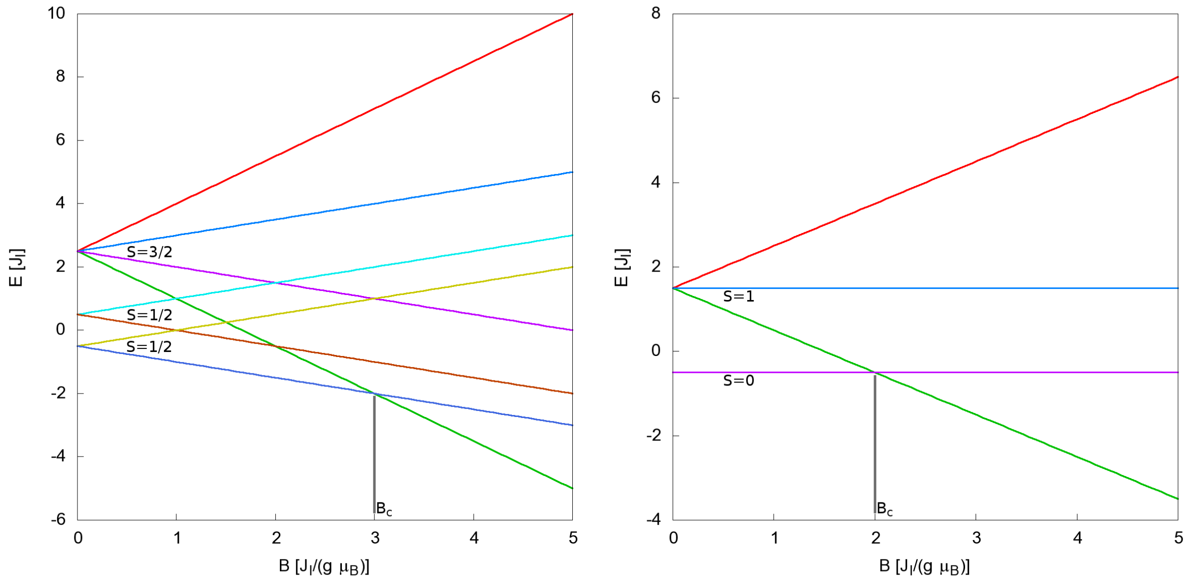

Figure 13: Sketch of the energy eigenvalues and their depence on the magnetic field for a free trimer chain (left) and a free dimer (right). The crossing fields B_c are marked. S is the total spin of the system.

Since we now want to study observables versus the external magnetic field, we choose to fix the temperature. To present the reader visually smooth curves, that mainly feature ground state contributions we use a temperature of about $2.032 \cdot 10^{-4} W/k_B$, which is roughly a magnitude below the intra-impurity couplings we will employ. With this information we look at figure 14. The first two graphs (red squares, empty grey squares) show the (impurity) magnetization for the free dimer and free trimer system. The figure also includes the crossing fields marked by vertical lines at $2 \cdot 10^{-3} W/(g\mu_B)$ and $3 \cdot 10^{-3} W/(g\mu_B)$ respectively. The other graphs then cover the complete range from the uncoupled or weakly coupled case to the strong coupling which is achieved for $J_A \gtrsim 0.5W$. While the case $J_A = 0W$ coincides with the free trimer (empty grey squares) by construction, the strongly coupled case (green crosses, purple triangles) coincides with the magnetization curve of a free dimer (red squares). The transition from weakly to strongly coupled case is also reflected in the crossing fields, which are given for several cases and can be derived from the magnetization. These vertical lines shift as the coupling is increased from the analytical solution of the free trimer to that of the free dimer. The analytical solutions thus are boundaries for the crossing field independent of the coupling J_A.

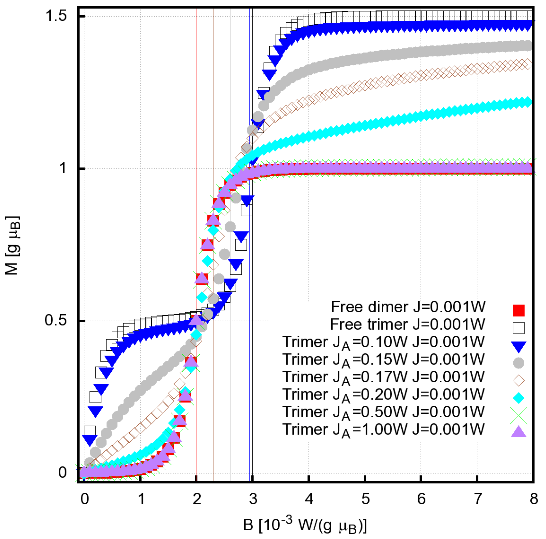

Figure 14: Impurity magnetization vs. external magnetic field for different parameter choices of a trimer (chain) system and a free dimer for comparison. The temperature is set to about $2.032 \cdot 10^{-4} W/k_B$. All graphs feature the same intra-impurity coupling with $J_I = 0.001W$. Beginning at the top of the key and going down, the first graph (red squares) shows a free dimer. The second graph (empty grey squares) belongs to a free trimer. For the third graph (blue triangles facing downwards) the coupling to the conduction band is set to $J_A = 0.1W$. The strength of this coupling to the conduction band increases for the following graphs. The fourth graph (grey circles) features $J_A = 0.15W$, the fifth graph (empty brown diamonds) $J_A = 0.17W$, the sixth graph (cyan diamonds) $J_A = 0.2W$ and the seventh graph (green crosses) $J_A = 0.5W$. The eighth and last graph (purple triangles) shows the trimer (chain) for $J_A = 1W$.

Further examining the strong coupling regime, figure 15 shows variations of the intra-impurity coupling in addition to those of the coupling to the conduction band. It should be noted, that within the regime the (impurity) magnetization versus the external magnetic field is (practically) independent of J_A and coincides with the solution for the free dimer. As the crossing field of the dimer is analytically dependent on the intra-impurity coupling $B_c = 2J_I/(g\mu_B)$, this relation is also true for the strongly coupled trimer, which is exemplarily demonstrated.

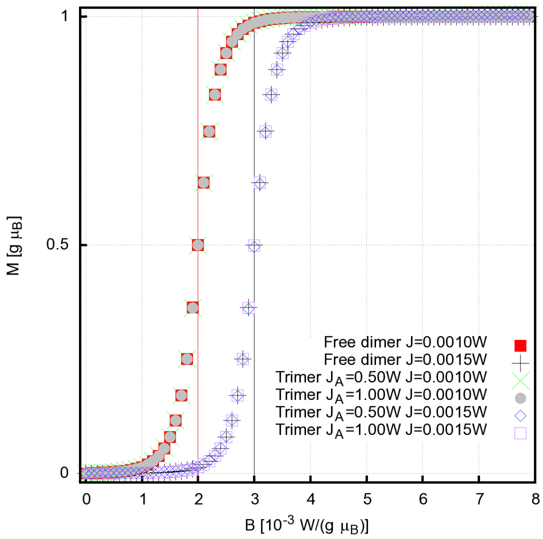

Figure 15: Impurity magnetization vs. external magnetic field for different parameter choices of a trimer (chain) system and of a free dimer system. The temperature is set to about $2.032 \cdot 10^{-4} W/k_B$. Beginning at the top of the key and going down, the first graph (red squares) shows a free dimer with intra-impurity coupling $J_I = 0.001W$. The second graph (black plus signs) features an intra-impurity coupling of $J_I = 0.0015W$. The third graph (green crosses) belongs to a trimer (chain) with intra-impurity interaction $J_I = 0.001W$ and a coupling to the conduction band $J_A = 0.5W$. For the fourth graph (grey circles) the coupling to the conduction band is set to $J_A = 1W$, while the intra-impurity interaction is unchanged at $J_I = 0.001W$. The fifth graph (empty blue diamonds) features the trimer (chain) system with an intra-impurity interaction $J_I = 0.0015W$ and a coupling to the conduction band $J_A = 0.5W$. The sixth and last graph (empty purple squares) shows the results for the trimer (chain) system with an intra-impurity interaction $J_I = 0.0015W$ and a coupling to the conduction band $J_A = 1W$.

Finally we take a look at a similar structure to the trimer chain in the form of a triangle with only one spin connected to the conduction band (see figure 16). For the free case we can use an analytical solution, as previously discussed in chapter 5.1, and show that the magnetization curves and thus the crossing fields coincide with that of the trimer chain for $T \to 0$. Since figure 17 however shows the magnetization curves (as before) for a finite temperature of about $2.032 \cdot 10^{-4} W/k_B$ the curves for $J_A = 0$ (red squares, blue triangles facing downwards) feature small differences. For intermediate couplings, as shown for $J_A = 0.15$ (grey circles, green diamonds) and $J_A = 0.2$ (brown triangles, purple squares), these differences are more distinct. This can especially be seen in the differences of the magnetization around values of the external magnetic field of roughly $B = 3.5 \cdot 10^{-3} W/(g\mu_B)$.

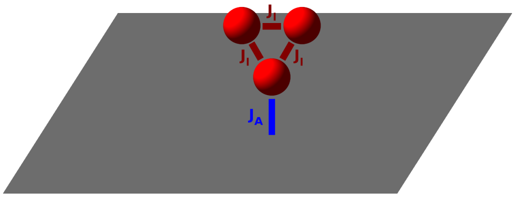

Figure 16: Sketch of a (trimer) triangle impurity (red) above a section of a lattice (grey) singly connected (blue) to a single lattice site. The full lattice extends indefinitely.

For the strong coupling regime, $J_A \gtrsim 0.5W$ just as we have established before, the magnetization curves (black crosses, cyan triangles) shown in figure 17 feature no visible differences and thus their crossing fields coincide. Similarly to the transition from trimer to dimer we can study such transitions starting from longer chains such as tetramer or pentamer chains. The magnetization curves for these systems show a similar transition as the magnetization curves of the trimer and can be found in the appendix chapter 8.2.

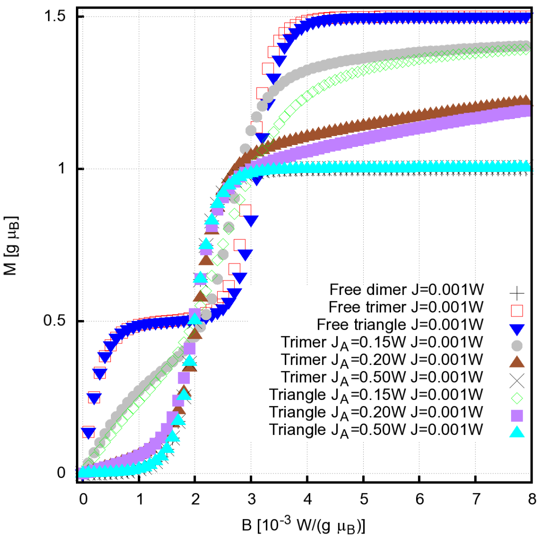

Figure 17: Impurity magnetization vs. external magnetic field for different parameter choices of a trimer (chain) system, of a (trimer) triangle system and of a free dimer system. The temperature is set to about $2.032 \cdot 10^{-4} W/k_B$. All graphs feature the same intra-impurity coupling with $J_I = 0.001W$. Beginning at the top of the key and going down, the first graph (black plus signs) shows a free dimer, the second graph (empty red squares) a free trimer (chain) and the third graph (blue triangle facing downwards) a free (trimer) triangle. The fourth graph (grey circles) belongs to a trimer (chain) with a coupling to the conduction band $J_A = 0.15W$. For the fifth graph (brown triangle) the coupling to the conduction band of this trimer (chain) is set to $J_A = 0.2W$. The sixth graph (black crosses) shows the trimer (chain) with a coupling to the conduction band of $J_A = 0.5W$. The seventh graph (empty green diamonds) is the first to feature the (trimer) triangle, with a coupling to the conduction band of $J_A = 0.15W$. For the eighth graph (purple squares) the coupling to the conduction band of this (trimer) triangle is set to $J_A = 0.2W$. Finally the ninth and last graph (cyan triangles) shows the results for the (trimer) triangle with a coupling to the conduction band $J_A = 0.5W$.

6 Discussion of involved scales

In the previous section we discussed a (doubly coupled) dimer system, a (triply coupled) trimer system, a trimer chain and a trimer triangle. We discussed the dimer system for different sets of parameters against changes of the temperature. Based on our observations there, we approached the (triply coupled) trimer system and again investigated the system for different sets of parameters against variations of the temperature. Due to our interest in some experimental observations we moved on to a fixed temperature but varied an outer magnetic field for our calculations of the trimer chain and trimer triangle. In discussing the different systems we were successful in identifying the different contributions to the observables of these systems and how they were influenced by the interaction with the conduction band.

Now we return to the bigger picture and take a look at the involved scales. In our first two systems we had the parameters and variables temperature, intra-impurity coupling and coupling to the conduction band. As it turned out, the coupling to the conduction band influences the interactions within the impurity via an indirect ferromagnetic interaction and also introduces the Kondo temperature as a potential scale. The intra-impurity interaction and the temperature are assosiated with a scale more directly. This means that we can identify three corresponding scales for our system. One is given by the effective interactions between the impurity spins, which ignoring the actual values of the spins can be estimated as:

$$\begin{aligned} \Omega_{J_I} &\approx 2J_{I,eff} && (68)\\ &\approx 2J_I \qquad for \;\; J_{indirect} \ll J_{ij}\ . && (69) \end{aligned}$$

A second is the scale of the Kondo temperature, which we have introduced in formula (2) before:

$$\Omega_{T_K} \approx k_B T_K \approx \sqrt{J_A/W}\exp\left(\frac{-1}{J_A/W}\right)\ . \qquad (70)$$

And a third is given by the scale of the temperature:

$$\Omega_T \approx k_B T \ , \tag{71}$$

which of course was varied for the calculation within a range encompassing the case of a temperature larger and smaller than both the other scales. For the other calculations we then introduced an additional scale in form of the outer magnetic field and the associated Zeeman term, which again ignoring the spin values may be approximated via:

$$\Omega_B \approx g\mu_B B \ . \tag{72}$$

For the systems in question we then fixed the temperature an order of magnitude below the scale of our interest, namely the scale of the intra-impurity interactions. It is important to remember, that we were specifically searching for a change in the crossing field. The crossing field is the strength of the external magnetic field, that needs to be applied to induce a transition in the groundstate of the system. Thus the magnetic field, while varied, was of comparable scale to the intra-impurity interactions. Due to all this, as we searched for a change in the crossing field of the system, we effectively varied Ω_{T_K} in comparison to Ω_{J_I}. With this in mind, the requirements for J_A to cause the change in crossing fields, that we had been looking for, can roughly be estimated via the ordering of scales in the system:

$$\Omega_T < \Omega_{J_I} \lesssim \Omega_B \ll \Omega_{T_K} \ , \tag{73}$$

which effectively means:

$$\Omega_{J_I} \ll \Omega_{T_K} \ , \tag{74}$$

so that we finally get to:

$$2J_I \ll \sqrt{J_A/W} \exp\left(\frac{-1}{J_A/W}\right) \ . \tag{75}$$

Based on our previous treatment of the Kondo temperature in chapter 2.4 and the tabulated values there, a first estimate for the required strength of the impurity-surface interaction J_A to induce a change in the crossing field via the strong coupling limit for the case $J_I = 0.001W$ would then be:

$$J_A \gg 0.2W \ , \tag{76}$$

which is consistent with our observation. It is noteworthy that we did not require any specific knowledge about the system to arrive at this conclusion. One must thus assume as a rule that such a change in crossing field via the strong coupling regime visible in the magnetization curves for nonmagnetic metallic substrates with half-bandwith W and deposited spin systems with internal interactions of a scale of $J_I = 0.001W$ can only be expected for impurity-surface interactions J_A of a scale larger than $0.2W$.

7 Summary

This thesis has presented numerical renormalization group calculations for the problem of spin clusters deposited on a nonmagnetic metallic substrate. The background for these calculations is the potential of depositing magnetic molecules on these nonmagnetic metallic substrates. Chapter 2 thus specifically has introduced the reader to the viewpoint of a researcher on magnetic molecules within the framework of Heisenberg Hamiltonians and statistical quantum mechanics. The same chapter has then presented the reader with an overview of the history of the Kondo model and the numerical renormalization group and linked both to the ongoing research of deposited molecules and quantum dots. In the following chapter 3 the theoretical framework has been summarized to enable the reader to comprehend the methodology and results of the later calculations. These calculations as shown in chapter 5 have first familiarized the reader with the relevant aspects of free dimer and trimer systems and then have shown effects of the Kondo screening on them. The chapter has focused specifically, as inspired by a related experiment, on the effects of the Kondo screening on the impurity magnetization curve of a trimer. The reader has been shown that a shift from a characteristically trimer-like to a dimer-like behavior in the impurity magnetization curve can be observed in the strong coupling regime for which a boundary condition in the form of the required strength of the impurity-surface interaction was given. The following chapter 6 has analyzed the involved scales in the problem. By doing this it has generalized the results by linking the required strength of the impurity-surface interaction to the intra-impurity interaction responsible for the crossing field, the strength of the external magnetic field, at which changes of the ground state occur. Due to this link one must assume as a rule that for molecules with internal interactions of strength $1meV$ (or on a choosable scale of the half-bandwith $0.001W$) and thus crossing fields of comparable strength a change to the strong coupling regime visible by a shift in the crossing field on magnetization curves is expected only for a strength of the impurity-surface interaction of a scale larger than $0.2eV$ (or on a choosable scale of the half-bandwith $0.2W$) given a half-bandwidth of the order of $1eV$ for the conduction band of the substrate. In the appendix this has been shown for magnetization curves of a tetramer and a pentamer chain. Finally the thesis has worked towards future research in the field by outlining the theoretical basics for numerical renormalization group calculations for two impurities on a square lattice surface that include the directional features of the surface. The theoretical framework was summarized in the excursus in chapter 4, while the important details of the calculations of the normalization factors haven been shown in the appendix.

8 Appendix

8.1 Calculation of the normalization factors

In our excursus in chapter 4 we discussed the density of states and the normalization factors in the context of including the features of a two dimensional square lattice into our calculations. The density of states was introduced in formula (10) as:

$$\rho(\epsilon) = \frac{1}{L^d} \sum_{\vec{k}} \delta(\epsilon - \epsilon_{\vec{k}}) \ .$$

In continuous momentum space in two dimensions it can be calculated via:

$$\rho(\epsilon) = \left(\frac{1}{2\pi}\right)^2 \cdot \int d^2k \cdot \delta(\epsilon - \epsilon(\vec{k})) \ , \tag{77}$$

with the solution as given in formula (52):

$$\rho(\epsilon) = \frac{1}{2 \cdot \pi^2 t} K\left(\tilde{m} = \tilde{k}^2 = [1 - \frac{\epsilon^2}{16 \cdot t^2}]\right) \ .$$

In chapter 4 I stated the importance of obtaining a suitable solution for the normalization factors, which were given in formulas (62) and (63) as:

$$\begin{aligned} N_e^2(\epsilon) &= 4 \int d\vec{k} \delta(\epsilon - \epsilon(\vec{k})) \cos^2(\vec{k} \cdot \vec{R}/2) \\ N_o^2(\epsilon) &= 4 \int d\vec{k} \delta(\epsilon - \epsilon(\vec{k})) \sin^2(\vec{k} \cdot \vec{R}/2) \ . \end{aligned}$$

It should be noted that these normalization factors feature an integral similar to the density of states but also include an additional trigonometrical factor. In the following I will explain a method of obtaining these normalization factors for a given value of $\vec{R}$, the distance vector between the sites at which two different impurities interact with the lattice. This distance vector is given in the form of integers counting the distance in multiples of the lattice spacing. The hopping parameter t is assumed to be positive.

8.1.1 Method

The method[2] as I present it in this and the next sub chapter focuses on solving the integral including the square cosine. With it and our solution for the density of states, we can easily obtain a solution for the sine via:

$$\sin^2 x = 1 - \cos^2 x \; . \tag{78}$$

The square cosine factor can be expanded by using trigonometrical identities to:

$$\begin{aligned}\cos^2\left(\frac{k_xR_x+k_yR_y}{2}\right) = \frac{1}{2} \;&+\; \frac{1}{8}(1-\cos(k_xR_x))(1-\cos(k_yR_y))\\ &-\; \frac{1}{8}(1+\cos(k_xR_x))(1-\cos(k_yR_y))\\ &-\; \frac{1}{8}(1-\cos(k_xR_x))(1+\cos(k_yR_y))\\ &+\; \frac{1}{8}(1+\cos(k_xR_x))(1+\cos(k_yR_y))\\ &-\; \frac{1}{2}\sin(k_xR_x)\sin(k_yR_y) \; .\end{aligned} \tag{79}$$

This can now be expanded further by using explicit values for R_x and R_y the integer components of the distance vector $\vec{R}$. The obtained form can again be expanded using trigonometric identities to reduce any multiplicities of the wave numbers (De Moivre's formula, see [62]). The result then features only sine and cosine over single wave numbers k_x and k_y and powers of these trigonometrical functions. We take note of the fact, that within the integrals as defined by (62) and (63) and with the dispersion relation (51) any odd term in an expansion of the original squared cosine will vanish due to symmetry. To understand this we take a look at the delta distribution using the formula [63]:

$$\int f(x)\delta(g(x))dx = \sum_i \frac{f(x_i)}{|g'(x_i)|} \; . \tag{80}$$

---

[2] It is important to note that the solution to the calculation of the integrals for these normalization factors as I present it here has been suggested to me in full by Apl. Prof. Dr. Heinz-Jürgen Schmidt, to whom I am most grateful for this.

Here the x_i are all the roots of the function $g(x)$, while $f(x)$ as a function encompasses additional multiplicative factors within the integral. For our problem at hand this means the $f(x)$ is of no relevance for the original dispersion relation and can be chosen to represent the trigonometrical factors in the calculation of the normalization factors. Of interest now are thus the roots of $g(x)$. To solve our two dimensional problem using this one dimensional formula, we define for simplicity that the x-axis is the direction for which we first perform the integration. Thus, based on formula (51), we need to find all roots for:

$$g(k_x) = \epsilon - \epsilon_{k_x,k_y} = \epsilon + 2t(\cos(k_x) + \cos(k_y)) \ . \tag{81}$$

We see that the roots depend on ϵ and the fixed values of k_y for which we attempt to solve the problem. To better understand the possible solutions the problem is visualized in figure (18) and (19) for positive and negative values of the energy ϵ respectively.

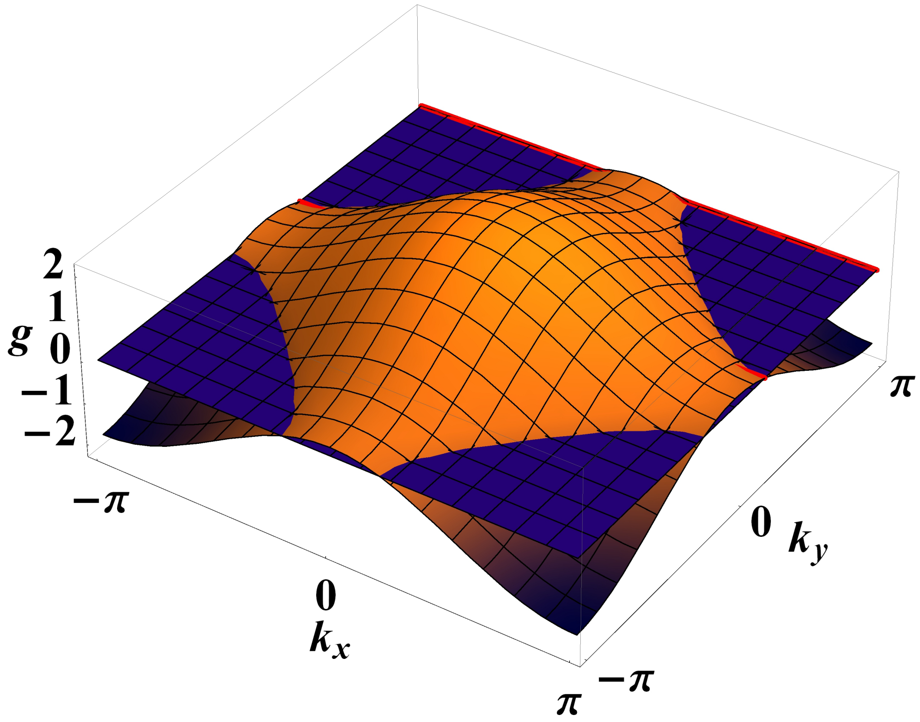

Figure 18: Intersection of zero level (purple) with $g(k_x, k_y)$ (orange colour gradient) for $\frac{\epsilon}{2t} = 0.2$. The red lines mark the range of positive k_y for which a solution for k_x in $g(k_x) = 0$ can be found.

As can be seen the problem is symmetric with respect to both axes and solutions for k_x exist only within a range of k_y depending on ϵ. Due to this, as remarked above, odd

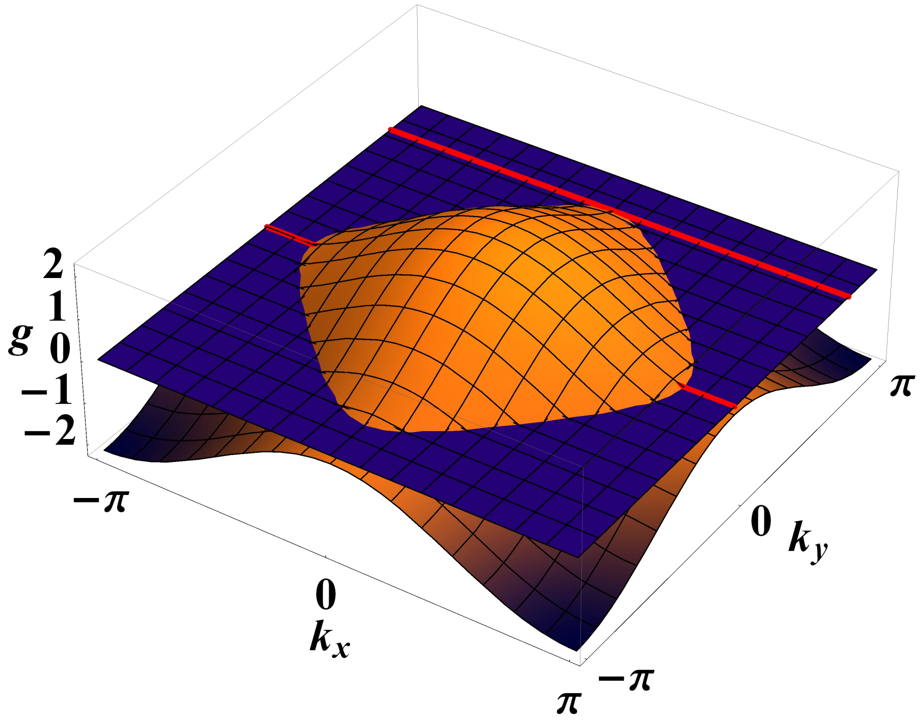

Figure 19: Intersection of zero level (purple) with $g(k_x, k_y)$ (orange colour gradient) for $\frac{\epsilon}{2t} = -0.2$. The red lines mark the range of positive k_y for which a solution for k_x in $g(k_x) = 0$ can be found.

terms in the function $f(x)$ like a sine do not contribute to the integral. This is of course true for any odd power of sine, while any even power of a sine can be replaced by the corresponding cosine. For all solutions $g(k_{xi}) = 0$, we find that $\cos(k_{xi}) = -\cos(k_y) - \frac{\epsilon}{2t}$ so that we can replace the cosine term in our calculations for formula (80). The limited range of k_y for which solutions exist furthermore leads to a limited range for which the integration along the y-axis needs to be performed, as the contribution to the integral is equal to zero outside that range. Putting our solution for the root into the derivative for $g(x_i)$ from formula (80) we get:

$$|g'(k_{xi})| = |-2t\sin(k_{xi})| = 2t\sqrt{1-\cos^2(k_{xi})} = 2t\sqrt{1-(cos(k_y)+\frac{\epsilon}{2t})^2}\,. \tag{82}$$

This derivative $g(k_{xi})$ encompasses the additional factor $\frac{1}{2}$ for the overall solution of the integral which we compensate by using the symmetry on the y-axis, so that our final range for the integral only encompasses positive values for k_y. We can visually identify these ranges in the figures (18) and (19) for positive and negative values of the energy ϵ respectively and mathematically they can be given as:

$$\begin{aligned} \text{for } \epsilon < 0 \quad &: 0 \quad \text{to} \quad k_- = \arccos(-1 - \frac{\epsilon}{2t}) \qquad (83) \\ \text{for } \epsilon > 0 \quad &: k_+ = \arccos(1 - \frac{\epsilon}{2t}) \quad \text{to} \quad \pi \; . \qquad (84) \end{aligned}$$

At this point it is important to note, that we gain an additional factor two due to the existence of two roots. We choose to move this factor outside the integral to avoid any confusion and will bring it up again when we arrive at the final solution. By separating any other constant factors from the cosine terms into another factor the (half-)integral can finally be expressed in the form:

$$I_{form} = \sum_n F_n I_n \; , \qquad (85)$$

with n corresponding to the power of $\cos(k_y)$, F_n a factor and the integral I_n given by:

$$I_n = \begin{cases} \frac{1}{t} \int_0^{k_-} \frac{\cos^n(k_y)}{\sqrt{1-(\cos(k_y)+\frac{\epsilon}{2t})^2}} dk_y & \text{with } k_- = \arccos(-1 - \frac{\epsilon}{2t}) \text{ for } \epsilon < 0 \\ \frac{1}{t} \int_{k_+}^{\pi} \frac{\cos^n(k_y)}{\sqrt{1-(\cos(k_y)+\frac{\epsilon}{2t})^2}} dk_y & \text{with } k_+ = \arccos(1 - \frac{\epsilon}{2t}) \quad \text{for } \epsilon > 0 \; . \end{cases} \qquad (86)$$

The normalization factor can then finally be obtained by including the factor four, originally outside the integral, and the factor two, resulting from the existence of two roots:

$$I_{norm} = 4 \cdot 2 \cdot \sum_n F_n I_n \; , \qquad (87)$$

Giving the explicit form leads us back to the elliptic integrals, so I_0, I_1 and I_2 for example can be expressed as:

$$I_0 = \frac{4K\left(\tilde{m} = \tilde{k}^2 = [1 - \frac{16 \cdot t^2}{\epsilon^2}]\right)}{|\epsilon|} \qquad (88)$$

$$I_1 = \frac{4t(K\left(\tilde{m} = \tilde{k}^2 = [1 - \frac{16 \cdot t^2}{\epsilon^2}]\right) - 2 \cdot \Pi\left(1 - \frac{4t}{|\epsilon|}, \tilde{m} = \tilde{k}^2 = [1 - \frac{16 \cdot t^2}{\epsilon^2}]\right))}{t\epsilon} \qquad (89)$$

$$\begin{aligned} I_2 = -\frac{1}{2t^2|\epsilon|} & \\ (\epsilon^2\cdot \quad & E \quad \left(\tilde{m} = \tilde{k}^2 = [1 - \frac{16\cdot t^2}{\epsilon^2}]\right) \\ +2(-4t^2+\epsilon^2+6t|\epsilon|)\cdot \quad & K \quad \left(\tilde{m} = \tilde{k}^2 = [1 - \frac{16\cdot t^2}{\epsilon^2}]\right) \qquad (90) \\ -24t|\epsilon|\cdot \quad & \Pi \quad \left(1 - \frac{4t}{|\epsilon|}, \tilde{m} = \tilde{k}^2 = [1 - \frac{16\cdot t^2}{\epsilon^2}]\right)) \ , \qquad (91) \end{aligned}$$

with E the complete elliptical integral of the second kind and Π the complete elliptical integral of the third kind. It is noteworthy, that for the complete elliptic integral of the first kind and thus I_0 the following is true:

$$I_0 = \frac{4K\left(\tilde{m} = \tilde{k}^2 = [1 - \frac{16\cdot t^2}{\epsilon^2}]\right)}{|\epsilon|} = \frac{K\left(\tilde{m} = \tilde{k}^2 = [1 - \frac{\epsilon^2}{16\cdot t^2}]\right)}{|t|} = \rho(\epsilon)\cdot 2\pi^2 \ , \qquad (92)$$

which can also be verified by using formula (87) with an outside factor of $\left(\frac{1}{2\pi}\right)^2$ instead of four and representing the trigonometrical factors only by $F_0 = 1$, while all other F_n are zero.

8.1.2 Examples

To expand on the sub chapter detailing the method, we make a simple example in the form of $R_x = 1$ and $R_y = 0$. Putting the values into formula (79) yields directly:

$$\cos^2\left(\frac{k_x}{2}\right) = \frac{1}{2} + \frac{\cos(k_x)}{2} \ . \qquad (93)$$

This form features neither multiples of wave numbers within a cosine nor a sine. Thus we do not need to expand it further. Performing the integration with the delta distribution leads practically to replacing $\cos(k_x)$ with $-\cos(k_y) - \frac{\epsilon}{2t}$ for these trigonometrical factors, while we keep the resulting factor two in mind for later. Thus we determine the factors F_n corresponding to the powers of $\cos(k_y)$ as:

$$\begin{aligned} F_0 &= \frac{1}{2} - \frac{\epsilon}{4t} && (94)\\ F_1 &= -\frac{1}{2}\,. && (95)\end{aligned}$$

The I_{form} is then according to formula (85):

$$\begin{aligned} I_{form} &= (\frac{1}{2} - \frac{\epsilon}{4t})\frac{4K\left(\tilde{m} = \tilde{k}^2 = [1 - \frac{16\cdot t^2}{\epsilon^2}]\right)}{|\epsilon|} && (96)\\ &-\frac{1}{2}\frac{4(K\left(\tilde{m} = \tilde{k}^2 = [1 - \frac{16\cdot t^2}{\epsilon^2}]\right) - 2\cdot\Pi\left(1 - \frac{4t}{|\epsilon|}, \tilde{m} = \tilde{k}^2 = [1 - \frac{16\cdot t^2}{\epsilon^2}]\right))}{\epsilon}\,, \end{aligned}$$

and thus the normalization factor itself:

$$\begin{aligned} N_e^2(\epsilon) &= I_{norm} = 8\cdot I_{form} && (97)\\ &= (\frac{1}{2} - \frac{\epsilon}{4t})\frac{32\cdot K\left(\tilde{m} = \tilde{k}^2 = [1 - \frac{16\cdot t^2}{\epsilon^2}]\right)}{|\epsilon|}\\ &-\frac{16(K\left(\tilde{m} = \tilde{k}^2 = [1 - \frac{16\cdot t^2}{\epsilon^2}]\right) - 2\cdot\Pi\left(1 - \frac{4t}{|\epsilon|}, \tilde{m} = \tilde{k}^2 = [1 - \frac{16\cdot t^2}{\epsilon^2}]\right))}{\epsilon}\,. \end{aligned}$$

As a second example we choose $R_x = 1$ and $R_y = 1$. Putting the values into formula (79) brings us to:

$$\begin{aligned} \cos^2\left(\frac{k_x + k_y}{2}\right) = \frac{1}{2} &+ \frac{1}{8}(1 - \cos(k_x))(1 - \cos(k_y))\\ &- \frac{1}{8}(1 + \cos(k_x))(1 - \cos(k_y))\\ &- \frac{1}{8}(1 - \cos(k_x))(1 + \cos(k_y))\\ &+ \frac{1}{8}(1 + \cos(k_x))(1 + \cos(k_y))\\ &- \frac{1}{2}\sin(k_x)\sin(k_y)\,. && (98)\end{aligned}$$

Here we now remove the sine and replace all $\cos(k_x)$ with $-\cos(k_y) - \frac{\epsilon}{2t}$, as before keeping in mind a factor two from the existence of two roots. Then we simplify until we arrive at:

$$
\begin{aligned}
F_0 &= \frac{1}{2} && (99)\\
F_1 &= -\frac{\epsilon}{4t} && (100)\\
F_2 &= -\frac{1}{2}\,. && (101)
\end{aligned}
$$

So that the normalization factor can finally be determined as:

$$
\begin{aligned}
N_e^2(\epsilon) &= I_{norm} = 8 \cdot I_{form} \qquad (102)\\
&= \frac{16K\left(\tilde{m} = \tilde{k}^2 = [1 - \frac{16 \cdot t^2}{\epsilon^2}]\right)}{|\epsilon|}\\
&\quad -\frac{8(K\left(\tilde{m} = \tilde{k}^2 = [1 - \frac{16 \cdot t^2}{\epsilon^2}]\right) - 2 \cdot \Pi\left(1 - \frac{4t}{|\epsilon|}, \tilde{m} = \tilde{k}^2 = [1 - \frac{16 \cdot t^2}{\epsilon^2}]\right))}{t}\\
&\quad +\frac{2}{t^2|\epsilon|}\\
&\qquad \Bigg[\epsilon^2 \cdot E\left(\tilde{m} = \tilde{k}^2 = [1 - \frac{16 \cdot t^2}{\epsilon^2}]\right)\\
&\quad +2(-4t^2 + \epsilon^2 + 6t|\epsilon|) \cdot K\left(\tilde{m} = \tilde{k}^2 = [1 - \frac{16 \cdot t^2}{\epsilon^2}]\right)\\
&\qquad -24t|\epsilon| \cdot \Pi\left(1 - \frac{4t}{|\epsilon|}, \tilde{m} = \tilde{k}^2 = [1 - \frac{16 \cdot t^2}{\epsilon^2}]\right)\Bigg]\,.
\end{aligned}
$$

8.2 Figures for the tetramer and pentamer chain

This part of the appendix shows magnetization curves for the tetramer (see figure 20) and pentamer chain (see figure 21). These are extensions of the trimer chain discussed in chapter 5.4. They show transitions similar to the trimer chain when affected by the screening of the strong coupling regime and can thus be understood by means of the previous analysis. To allow for a better distinction of the several plateaus in the magnetization a temperature of about $5.9610 \cdot 10^{-8} W/k_B$ was chosen.

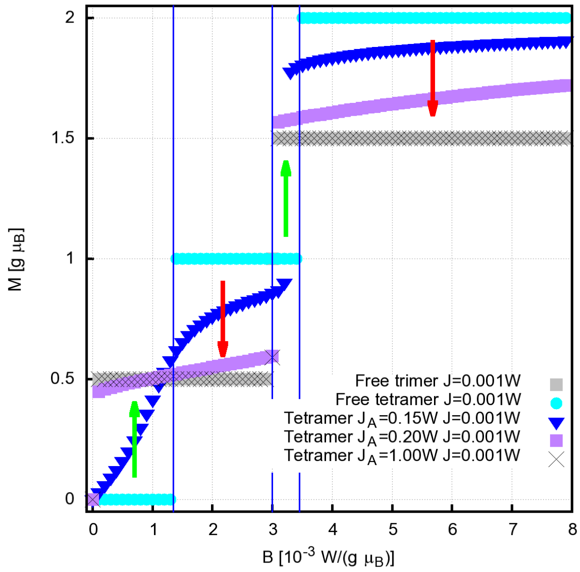

Figure 20: Impurity magnetization vs. external magnetic field for different parameter choices of a tetramer (chain) system and a free trimer (chain) for comparison. The temperature is set to about $5.9610 \cdot 10^{-8} W/k_B$. The vertical lines separate different regimes of the external magnetic field, for which the transition of the tetramer from the free to the strongly coupled case leads to either an increase (green arrow) or decrease (red arrow) in the magnetization. All graphs feature the same intra-impurity coupling with $J_I = 0.001W$. Beginning at the top of the key and going down, the first graph (grey squares) shows a free trimer (chain) and the second graph (cyan circles) a free tetramer (chain). The third graph (blue triangles facing downwards) features the tetramer (chain) with a coupling to the conduction band of $J_A = 0.15W$. For the fourth graph (purple squares) the coupling to the conduction band of this tetramer (chain) is set to $J_A = 0.2W$. Finally the fifth and last graph (black crosses) shows the results for the tetramer (chain) with a coupling to the conduction band $J_A = 1W$.

Graphs for intermediate couplings (in both figures: blue triangles facing downwards, purple squares) are given to illustrate the transition. They however are not characterized by the same regimes of the external magnetic field that the free and the strongly coupled case are characterized by.

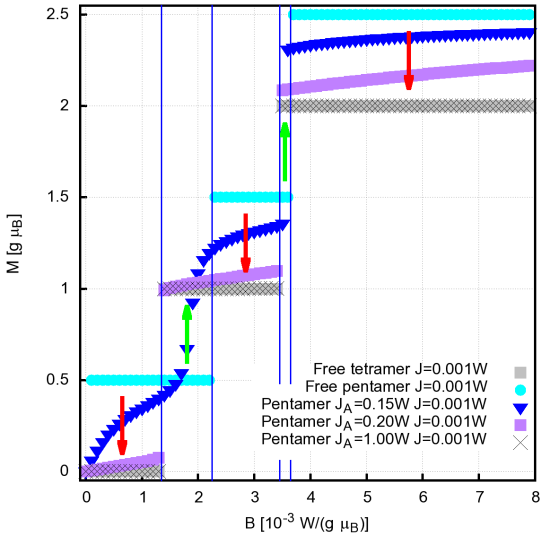

Figure 21: Impurity magnetization vs. external magnetic field for different parameter choices of a pentamer (chain) system and a free tetramer (chain) for comparison. The temperature is set to about $5.9610 \cdot 10^{-8} W/k_B$. The vertical lines separate different regimes of the external magnetic field, for which the transition of the pentamer from the free to the strongly coupled case leads to either an increase (green arrow) or decrease (red arrow) in the magnetization. All graphs feature the same intra-impurity coupling with $J_I = 0.001W$. Beginning at the top of the key and going down, the first graph (grey squares) shows a free tetramer (chain) and the second graph (cyan circles) a free pentamer (chain). The third graph (blue triangles facing downwards) features the pentamer (chain) with a coupling to the conduction band of $J_A = 0.15W$. For the fourth graph (purple squares) the coupling to the conduction band of this pentamer (chain) is set to $J_A = 0.2W$. Finally the fifth and last graph (black crosses) shows the results for the pentamer (chain) with a coupling to the conduction band $J_A = 1W$.

References

[1] D. Gatteschi, R. Sessoli, and J. Villain. *Molecular nanomagnets*. Oxford Univ. Press, 2006.

[2] J. Schnack. Molecular magnetism. In U. Schollwöck, J. Richter, D. J. J. Farnell, and R. F. Bishop, editors, *Quantum Magnetism*, pages 155–194. Springer Berlin Heidelberg, Berlin, Heidelberg, 2004.

[3] C. A. P. Goodwin, F. Ortu, D. Reta, N. F. Chilton, and D. P. Mills. Molecular magnetic hysteresis at 60 kelvin in dysprosocenium. *Nature*, 548:439–442, 2017.

[4] R. Sessoli. Toward the Quantum Computer: Magnetic Molecules Back in the Race. *ACS Cent. Sci.*, 1(9):473–474, 2015.

[5] J. Wiebe, L. Zhou, and R. Wiesendanger. Atomic magnetism revealed by spin-resolved scanning tunnelling spectroscopy. *J. Phys. D*, 44(46):464009, 2011.

[6] M. Höck. *Numerical Renormalization Group calculations of the magnetization of Kondo impurities*. PhD thesis, 2013.

[7] J. Kondo. Resistance Minimum in Dilute Magnetic Alloys. *Prog. Theor. Phys.*, 32(1):37–49, 1964.

[8] W. J. de Haas, J. de Boer, and G. J. van dën Berg. The electrical resistance of gold, copper and lead at low temperatures. *Physica*, 1(7):1115 – 1124, 1934.

[9] C. Zener. Interaction Between the d Shells in the Transition Metals. *Phys. Rev.*, 81:440–444, 1951.

[10] T. Kasuya. A Theory of Metallic Ferro- and Antiferromagnetism on Zener's Model. *Prog. Theor. Phys.*, 16(1):45–57, 1956.

[11] K. Yosida. Magnetic Properties of Cu-Mn Alloys. *Phys. Rev.*, 106:893–898, 1957.

[12] K. Yosida. Anomalous Electrical Resistivity and Magnetoresistance Due to an $s-d$ Interaction in Cu-Mn Alloys. *Phys. Rev.*, 107:396–403, 1957.

[13] P. W. Anderson. Localized Magnetic States in Metals. *Phys. Rev.*, 124:41–53, 1961.

[14] P. A. Wolff. Localized Moments in Metals. *Phys. Rev.*, 124:1030–1035, 1961.

[15] J. R. Schrieffer and P. A. Wolff. Relation between the Anderson and Kondo Hamiltonians. *Phys. Rev.*, 149:491–492, 1966.

[16] P. W. Anderson. A poor man's derivation of scaling laws for the Kondo problem. *J. Phys. C*, 3(12):2436, 1970.

[17] K. G. Wilson. The renormalization group: Critical phenomena and the Kondo problem. *Rev. Mod. Phys.*, 47:773–840, 1975.

[18] A. C. Hewson. *The Kondo Problem to Heavy Fermions*. Cambridge Studies in Magnetism. Cambridge University Press, 1993.

[19] H. R. Krishna-murthy, J. W. Wilkins, and K. G. Wilson. Renormalization-group approach to the Anderson model of dilute magnetic alloys. I. Static properties for the symmetric case. *Phys. Rev. B*, 21:1003–1043, 1980.

[20] H. R. Krishna-murthy, J. W. Wilkins, and K. G. Wilson. Renormalization-group approach to the Anderson model of dilute magnetic alloys. II. Static properties for the asymmetric case. *Phys. Rev. B*, 21:1044–1083, 1980.

[21] R. Bulla, T. A. Costi, and T. Pruschke. Numerical renormalization group method for quantum impurity systems. *Rev. Mod. Phys.*, 80:395–450, 2008.

[22] W. C. Oliveira and L. N. Oliveira. Generalized numerical renormalization-group method to calculate the thermodynamical properties of impurities in metals. *Phys. Rev. B*, 49:11986–11994, 1994.

[23] V. L. Campo and L. N. Oliveira. Thermodynamics for the two-impurity Kondo model. *Phys. Rev. B*, 70:153401, 2004.

[24] V. L. Campo and L. N. Oliveira. Alternative discretization in the numerical renormalization-group method. *Phys. Rev. B*, 72:104432, 2005.

[25] R. Žitko and T. Pruschke. Energy resolution and discretization artifacts in the numerical renormalization group. *Phys. Rev. B*, 79:085106, 2009.

[26] R. Žitko. Adaptive logarithmic discretization for numerical renormalization group methods. *Comput. Phys. Commun.*, 180(8):1271 – 1276, 2009.

[27] A. K. Mitchell, M. R. Galpin, S. Wilson-Fletcher, D. E. Logan, and R. Bulla. Generalized Wilson chain for solving multichannel quantum impurity problems. *Phys. Rev. B*, 89:121105, 2014.

[28] B. Lechtenberg and F. B. Anders. Spatial and temporal propagation of Kondo correlations. *Phys. Rev. B*, 90:045117, 2014.

[29] M. F. Crommie, C. P. Lutz, and D. M. Eigler. Spectroscopy of a single adsorbed atom. *Phys. Rev. B*, 48:2851–2854, 1993.

[30] V. Madhavan, W. Chen, T. Jamneala, M. F. Crommie, and N. S. Wingreen. Tunneling into a Single Magnetic Atom: Spectroscopic Evidence of the Kondo Resonance. *Science*, 280(5363):567–569, 1998.

[31] J. Li, W.-D. Schneider, R. Berndt, and B. Delley. Kondo Scattering Observed at a Single Magnetic Impurity. *Phys. Rev. Lett.*, 80:2893–2896, 1998.

[32] F. Meier, L. Zhou, J. Wiebe, and R. Wiesendanger. Revealing Magnetic Interactions from Single-Atom Magnetization Curves. *Science*, 320(5872):82–86, 2008.

[33] A. A. Khajetoorians, S. Lounis, B. Chilian, A. T. Costa, L. Zhou, D. L. Mills, J. Wiebe, and R. Wiesendanger. Itinerant nature of atom-magnetization excitation by tunneling electrons. *Phys. Rev. Lett.*, 106:037205, 2011.

[34] H. Brune and P. Gambardella. Magnetism of individual atoms adsorbed on surfaces. *Surf. Sc.*, 603(10):1812 – 1830, 2009.

[35] L. Zhou, J. Wiebe, S. Lounis, E. Vedmedenko, F. Meier, S. Blugel, P. H. Dederichs, and R. Wiesendanger. Strength and directionality of surface Ruderman-Kittel-Kasuya-Yosida interaction mapped on the atomic scale. *Nat. Phys.*, 6(3):187–191, 2010.

[36] A. A. Khajetoorians, J. Wiebe, B. Chilian, S. Lounis, S. Blügel, and R. Wiesendanger. Atom-by-atom engineering and magnetometry of tailored nanomagnets. *Nat. Phys.*, 8:497–503, 2012. Article.

[37] M. Mannini, F. Pineider, P. Sainctavit, C. Danieli, E. Otero, C. Sciancalepore, A. M. Talarico, M.-A. Arrio, A. Cornia, D. Gatteschi, and R. Sessoli. Magnetic memory of

a single-molecule quantum magnet wired to a gold surface. *Nat. Mat.*, 8:194–197, 2009.

[38] M. Bernien, J. Miguel, C. Weis, Md. E. Ali, J. Kurde, B. Krumme, P. M. Panchmatia, B. Sanyal, M. Piantek, P. Srivastava, K. Baberschke, P. M. Oppeneer, O. Eriksson, W. Kuch, and H. Wende. Tailoring the Nature of Magnetic Coupling of Fe-Porphyrin Molecules to Ferromagnetic Substrates. *Phys. Rev. Lett.*, 102:047202, 2009.

[39] X. Chen, Y.-S. Fu, S.-H. Ji, T. Zhang, P. Cheng, X.-C. Ma, X.-L. Zou, W.-H. Duan, J.-F. Jia, and Q.-K. Xue. Probing Superexchange Interaction in Molecular Magnets by Spin-Flip Spectroscopy and Microscopy. *Phys. Rev. Lett.*, 101:197208, 2008.

[40] A. K. Mitchell, D. E. Logan, and H. R. Krishnamurthy. Two-channel Kondo physics in odd impurity chains. *Phys. Rev. B*, 84:035119, 2011.

[41] A. K. Mitchell, E. Sela, and D. E. Logan. Two-Channel Kondo Physics in Two-Impurity Kondo Models. *Phys. Rev. Lett.*, 108:086405, 2012.

[42] A. K. Mitchell, T. F. Jarrold, M. R. Galpin, and D. E. Logan. Local Moment Formation and Kondo Screening in Impurity Trimers. *J. Phys. Chem. B*, 117(42):12777–12786, 2013.

[43] S. B. Tooski, B. R. Bułka, R. Žitko, and A. Ramšak. Entanglement switching via the Kondo effect in triple quantum dots. *Eur. Phys. J. B*, 87(6):145, 2014.

[44] R. Žitko and J. Bonca. Enhanced conductance through side-coupled double quantum dots. *Phys. Rev. B*, 73:035332, 2006.

[45] R. Žitko and J. Bonca. Numerical renormalization group study of two-channel three-impurity triangular clusters. *Phys. Rev. B*, 77:245112, 2008.

[46] R. Žitko. Fano-Kondo effect in side-coupled double quantum dots at finite temperatures and the importance of two-stage Kondo screening. *Phys. Rev. B*, 81:115316, 2010.

[47] M. Höck and J. Schnack. Numerical renormalization group calculations of the magnetization of Kondo impurities with and without uniaxial anisotropy. *Phys. Rev. B*, 87:184408, 2013.

[48] L. Borda. Kondo screening cloud in a one-dimensional wire: Numerical renormalization group study. *Phys. Rev. B*, 75:041307, 2007.

[49] J. Kondo. Theory of Dilute Magnetic Alloys. volume 23 of *Solid State Physics*, pages 183 – 281. Academic Press, 1970.

[50] R. Žitko. *Many-particle effects in resonant tunneling of electrons through nanostructures*. PhD thesis, 2007.

[51] E. Jensen and E. W. Plummer. Experimental Band Structure of Na. *Phys. Rev. Lett.*, 55:1912–1915, 1985.

[52] S. Hüfner. Bandwidth of free electron metals as measured by photoelectron spectroscopy. *Solid State Commun.*, 59(9):639 – 641, 1986.

[53] P. J. Mohr, D. B. Newell, and B. N. Taylor. CODATA recommended values of the fundamental physical constants: 2014. *Rev. Mod. Phys.*, 88:035009, 2016.

[54] B. A. Jones and C. M. Varma. Study of two magnetic impurities in a Fermi gas. *Phys. Rev. Lett.*, 58:843–846, 1987.

[55] B. A. Jones, C. M. Varma, and J. W. Wilkins. Low-Temperature Properties of the Two-Impurity Kondo Hamiltonian. *Phys. Rev. Lett.*, 61:125–128, 1988.

[56] R. Piasecki. Density of electron states in a rectangular lattice under uniaxial stress. *ArXiv e-prints*, 2008.

[57] R. Steinigeweg and H.-J. Schmidt. Heisenberg-Integrable Spin Systems. *Math. Phys. Anal. Geom.*, 12(1):19–45, 2009.

[58] M. Vojta, R. Bulla, and W. Hofstetter. Quantum phase transitions in models of coupled magnetic impurities. *Phys. Rev. B*, 65:140405, 2002.

[59] R. Žitko. Kondo screening in high-spin side-coupled two-impurity clusters. *J. Phys. Condens. Matter*, 22(2):026002, 2010.

[60] H.-J. Schmidt, J. Schnack, and M. Luban. Heisenberg exchange parameters of molecular magnets from the high-temperature susceptibility expansion. *Phys. Rev. B*, 64:224415, 2001.

[61] A. K. Mitchell, T. F. Jarrold, and D. E. Logan. Quantum phase transition in quantum dot trimers. *Phys. Rev. B*, 79:085124, 2009.

[62] E. Zeidler, editor. *Springer-Taschenbuch der Mathematik*. Springer, 3rd edition, 2013.

[63] S. Hassani. *Mathematical Methods*. Springer, 2nd edition, 2009.